

Competition between cooling and shortwave radiation in shaping near-surface convection in pelagic waters of Lake Geneva



présenté le 7 Juillet 2021
à la Faculté de l'ENAC
laboratoire APHYS
Projet de master
École Polytechnique Fédérale de Lausanne
pour l'obtention du grade de Master
par

Hugo Cruz

acceptée sur proposition du jury:

Superviseurs de thèse Hugo Ulloa, Sebastiano Piccolroaz, Prof. Alfred J. Wüest

Lausanne, EPFL, 2021

Abstract

When lake surface waters above the temperature of maximum density 4°C cools, the very surface fluid parcels become denser than their neighbours below. The latter process leads to a gravitationally unstable density distribution which may trigger ‘free convection’, i.e. the upper denser waters look for their equilibrium position somewhere down in the water column. This phenomenon usually occurs at night time, when the atmosphere is colder than surface waters. However, during daytime, it may happen that the lake surface cools—releasing heat to the atmosphere—while shortwave radiation penetrates through upper waters. In this scenario, the near surface waters of the photic zone can host an unstable layer due to the net surface cooling, whereas waters beneath it experience radiative heating and gravitational stabilization. Here, we investigate the competition between shortwave radiation and surface cooling when wind is low or negligible. Thus, depending on the relative intensity of surface cooling and shortwave radiation, the upper water column undergoes different gravitationally unstable density distributions and potentially convective regions.

The objective of this Master Project is to investigate, describe, and characterise such convective regimes. To do so, the heat equation controlling temperature evolution of the upper water column subject to surface cooling and penetrative radiative heating is investigated. In parallel with in-situ observations, mathematical and numerical modelling allow to understand the phenomenon taking place. The results allow to infer how the relative importance of surface cooling and penetrating shortwave radiation may affect vertical heat and mass transfer within the lake and between the lake and the atmosphere.

Key words: Convection, temperature above 4°C , shortwave radiation, surface cooling

Contents

Abstract (English/Français/Deutsch)	i
List of figures	v
1 Introduction	1
1.1 Motivation	1
1.1.1 Physics motivation & State of the art	1
2 Study site and Data	5
2.1 Meteorological station	5
2.2 Heat fluxes	6
2.3 Temperature chain	6
2.4 Light extinction length scale λ	7
2.5 Short-term data: μ CTD profiler	7
3 Methods	9
3.1 Governing equations	9
3.1.1 Problem scales	10
3.2 Steady state solution	13
3.2.1 Compensation depth	14
3.2.2 Analytical Mixing depth at steady state conditions	15
3.3 Numerical modelling	17
3.3.1 Simple 1D implicit model	17
3.3.2 Time & spatially dependent parameters	19
3.3.3 Empirical Mixing depth algorithm	20
3.4 Model and μ CTD temperature profiles comparison	21
3.4.1 Model skill metric (MSM)	22
3.5 Statistical Analysis	22
3.5.1 Mixing layer depth estimation with temperature chain	23
3.6 Cloud cover	24
4 Results	25
4.1 Steady state	25
4.1.1 Building intuition	25

4.1.2	Steady state model	27
4.2	Timescales	29
4.3	μ CTD Profiles	30
4.4	Statistical analysis	33
4.4.1	Annual statistics	33
4.4.2	Consecutive events within a day	35
4.4.3	Daily statistics	37
4.4.4	Empirical based transition regime	37
4.5	Numerical model	40
5	Discussion	45
5.1	Steady State solution interpretation and its limitations	45
5.2	Timescales	46
5.3	μ CTD temperature profiles	46
5.4	Numerical model interpretation and limitations	47
5.5	Statistical analysis	48
6	Conclusion	51
7	Acknowledgements	53
	Bibliography	57

List of Figures

2.1	Lake Geneva. The red point shows the position of the LéXPLORE platform. . . .	5
3.1	Model grid for discretization of the heat equation at a time t	19
3.2	Click on the figure to animate it. This figure shows the mixing layer algorithm. The blue curve is the temperature profile, T is the actual temperature for a given temperature, \tilde{T} is the mean temperature from the surface to the reference depth. The vertical line on the right show the respective position of T with \tilde{T} . When the two points crosses each other, the algorithm stop and the depth is recorded as the mixing depth.	21
4.1	Schematic of the shortwave radiation and surface cooling respective importance in a day. The parameter R is the ratio of the kinematic surface heat flux Q_0 to the surface radiative flux I_0	26
4.2	Temperature profiles across different regimes: a) steady state solution \tilde{T} (eq. 3.25), b) stable mixed profile \tilde{T}_{mix} (eq. 3.37), and c) the above profiles compared with the progressively averaged profile \tilde{T}_{avg} (eq. 3.31). \tilde{T}_{norm} is the normalized non dimensional temperature \tilde{T} varying between 0 and 1 (for plotting purposes). The 2 filled black lines in a) and b) is the resulting steady state solution for $R = 0$ and $R = 1$. The black and red dashed line in a) and b) are the compensation depth \tilde{h}_c and mixing depth \tilde{h}_m	28
4.3	Heat timescales. τ_H/τ_C represent the ratio of the two timescales corresponding to shortwave radiation (τ_H) and surface cooling (τ_C). h is the reference depth, here represented as the mixing depth. λ is the light extinction length scale. The blue line with the points switching from grey to black gives an idea of how the system is changing within a day.	29
4.4	Click on the figure to animate it, hold to pause. μ CTD structure of temperature on the 18th of january 2021. The orange line is the raw data of temperature from the high resolution measurement. Grey line is the smoothed temperature using the Savitzky-Golay filter (Savitzky, 1964). Meteorological station and Heat fluxes are provided at each timestep. Wind is in ms^{-1} , H_0 and H_{SW} are in W m^{-2} . . .	31

4.5	The Polar Chart is separated into four distinct timelines. Each dots represents an event of 10 minutes where specific conditions are satisfied. An event is represented when there is: no wind (less than 2 ms), the lake is not stratified (the depth of the mixing layer is more than 5 m), N is the number of occurrences in each seasons: winter (JFM), spring (AMJ), summer (JAS) and autumn (OND).	34
4.6	Each bar is a day in which at one or multiple events took place. The radial axis is the time in hours of the events in a day. The more events there is within a day, the longer will be the bar. if conditions are fulfilled continuously in a day, the bar is filled in red.	36
4.7	Daily Statistics for each seasons. Occurrences refer to the number of 10 min events where the transition regime conditions are fulfilled. These plots are smoothed using a Savitzky–Golay filter with a window size of 9 and a polynomial order 3.	37
4.8	Updated polar chart (figure 4.5) considering $R \in [0.8; 2]$	38
4.9	Updated polar bar (figure 4.6) considering $R \in [0.8; 2]$	39
4.10	Daily statistics for the empirical R range ($R \in [0.8; 2]$)	40
4.11	Click to animate, hold to pause. Measured (solid black) temperature profile is shown. In parallel, the dotted and dashdotted black curves corresponds to the the temperature profile where the mixing algorithm is applied at every timestep and τ_{conv} respectively. The dashed black curve corresponds to the temperature profile without any mixing. The red dashed line corresponds to the smoothed turbulent diffusivity from measurements. The R ratio, surface cooling, shortwave radiation and wind are also displayed at the time when the modelled and measured temperature are plotted. Light extinction depth is set as $\lambda = 5m$ As the time resolution is set at one minute, no more than one minute is elapsed between the modelled profiles and the measured one.	42

1 Introduction

1.1 Motivation

1.1.1 Physics motivation & State of the art

Convection is defined as motions that result from the action of gravity upon an unstable density distribution in a fluid. Known as partly controlling mixing and stratification of the water column, it is thereby an important mechanism driving vertical fluxes and transport (Bouffard and Wüest, 2019; Imboden and Wüest, 1995). Being able to understand the physical parameters driving convection is a key point to characterise gas exchange and biological migration (Schwefel et al., 2016; Verburg et al., 2003). The convective mixed depth, here also defined as the mixing depth, is therefore an essential parameter in terms of physical and biological understanding of a lake.

Convective regimes are forced by energy exchange with the atmosphere. Heat fluxes characterization therefore plays a major role in lake hydrodynamics (Laird and Kristovich, 2002). In this study, surface cooling and penetrating solar radiation are studied in particular because of their opposing effect and their relative importance in determining water surface temperature i.e convective regimes (Piccolroaz et al., 2013). It is assumed that penetrative cooling causes mixing and deepening of the surface layer when thermal expansion coefficient $\alpha > 0$, while solar radiation is in general responsible for stabilizing the water column and leading to stratification.

On a seasonal timescale, convective regimes have been studied broadly in limnic researches (Boehrer and Schultze, 2008, Kirillin and Shatwell, 2016). On a daily timescale, change in forcing conditions influencing convection is often investigated in shallow lakes (Andersen et al., 2017, Augusto-Silva et al., 2019) or in the surface ocean (Sutherland et al., 2014). The seasonal mixed layer is defined as a layer extending from the surface to the region of maximum gradient of temperature in the metalimnion (Niiler, 1977). Closely related to the diurnal mixed layer, the seasonal mixed layer may be thought as an accumulation of past diurnal mixed layer events (Imberger and Hamblin, 1982). Imberger (1985) gives a first detailed analysis on the

diurnal mixed layer via microstructure analysis under three conditions: a morning period of solar heating, a period of severe wind mixing induced by an afternoon sea breeze, and a period of pure penetrative convection extending through most of the night. Since, the near-surface lake waters subjected to surface cooling and solar radiation in monomictic lakes is still an overlooked phenomenon.

More recent studies, like Soloviev and Lukas (2014), use a renewal air-sea gas transfer model to produce temperature profiles considering surface cooling, solar radiation and wind in an oceanic system (Soloviev and Schlüssel, 1996). The model focuses on the first centimeters of the surface boundary layer (Wüest and Lorke, 2003), also referred to as the "cool skin". It resulted that the main effect of solar radiation on the cool skin is observed at low wind speeds, and ensue a suppression of free convection due to the absorption of solar radiation having a strong effect on the gas transfer at the ocean-air interface. Given that wind forcing is usually weaker in lakes than in the ocean (Bouffard and Wüest, 2019), it is expected that solar radiation will have a larger impact on free convection.

Convective regimes are commonly described in a discrete way; a stratified regime implicitly implies that surface cooling is negligible (i.e. at midday), and a mixed regime implies that shortwave radiation is negligible (i.e. at night). By adopting a simple approach on a daily timescale, the relative importance of surface cooling with radiative heating is investigated in particular when these two are in competition, and may result in a complex convective regime, here named transition regime. Given that solar radiation penetrates through the water column acting as a volumetric source and surface cooling acts as a boundary flux (Bouffard and Wüest, 2019), the resulting temperature change may have their own signatures at different depths of the water column.

This present work is therefore focusing on the characterization and understanding of the diurnal mixing depth subjected to shortwave radiation and surface cooling under low or negligible wind forcing in the pelagic region. Lake Geneva is the largest freshwater lake in Western Europe and is considered as a deep perialpine lake. It is a warm monomictic lake with deepest seasonal mixing in late February/early March (Schwefel et al., 2016).

To characterize and understand these convective regimes under competitive forcing conditions, the diurnal mixing layer of lake Geneva is studied following the structure below.

To understand how the system reacts under comparable shortwave and cooling heat fluxes, microstructure data are analysed for a winter day in which the convective regime switches from a fully mixed to stratified regime.

A first analytical approach is given to the comprehension of the different convective regimes by finding a steady state solution using solar radiation and surface cooling as main drivers. At a daily scale, a simple analytical non-dimensional expression of the temperature field, diurnal mixing and compensation depth is established.

A better understanding and estimation is given to the effect of the shortwave radiation and cooling heat fluxes on the water column by investigating timescales involved in the physical processes under different forcing conditions and mixing layer properties.

To make a parallel between the mathematical understanding and the observations made, a

simple 1D numerical model is created and adapted to constantly changing meteorological and mixing conditions in time. Additionally a simple mixing algorithm is implemented. A critical study on the assumptions considered and the possible missing parameters or physical processes in the model implementation are also investigated.

Finally, a statistical analysis on an annual scale is evaluated, based on long-term data with a characterisation in time and persistency of the convective regime in question allowing to infer the relative importance of the phenomenon studied.

2 Study site and Data

The LÉXPLORE platform is a 10 m by 10 m pontoon equipped with high-tech instrumentation and situated 570 m from the shoreline of Pully (46°30'0.819" N and 6°39'39.007" E). (Wüest et al., 2021). The data collected at the LÉXPLORE platform are available via the Datalakes website, an open access data management platform for lake-related environmental data and products. Data used in the frame of this thesis are exported from Datalakes and processed during the period from April 2020 to April 2021. Long-term datasets are here considered as measurements taken continuously during the entire year with a time resolution of 10 minutes.



Figure 2.1 – Lake Geneva. The red point shows the position of the LÉXPLORE platform.

2.1 Meteorological station

A meteorological station is mounted on the platform 5 m above water level. The station is composed of 5 sensors:

- An anemometer to measure wind speed and direction
- Apogee PYR-P Pyranometer to acquire solar radiations
- Rotronic HygroCL1P2 Temp and relative Humidity Probe to measure air temperature and relative humidity
- Barometric Sensor 600 to 1100 mB to measure atmospheric pressure
- Raingauge to measure rainfall

The meteorological station, following the standard meteorological, is making an average after a 10 min measurement, thus providing information of the past. Measurements are imported and shifted by 10 min in order to have present measurements.

During the data processing, the season for each measurement is also specified. Months were grouped according to the standard climatological seasons: winter (January, February and March, JFM), spring (April, May, June, AMJ), summer (July, August, September, JAS) and fall (October, November, December, OND).

2.2 Heat fluxes

Heat fluxes are obtained via empirical equations (Fink et al., 2014), calculated and exported at each 10 min timestep via the Datalakes website.

H_0 is defined as the surface cooling heat flux component (defined positive when the water surface is cooling): $H_0 = H_T + H_E + H_{LW}$ where H_T , H_E , H_{LW} denote the sensible, latent and the net longwave irradiance heat flux respectively. H_{SW} is the shortwave radiation heat flux at the surface of the water column (defined positive). H_{net} denotes the net surface heat flux and can be defined as $H_{net} = H_0 - H_{SW}$, defined positive when the lake is cooling.

2.3 Temperature chain

The platform has a temperature chain that provides temperature every 10 min at discrete depths. The temperature chain is separated in two:

- The first chain has a 20 m length with 24 RBR temperature sensors. A sensor is fixed at a depth of 0.25 m, 0.5 m, 1 m, 1.5 m, 2 m, 2.5 m, 3 m and then every meter down to a depth of 18 m.
- The second chain has a 70 m length with 24 RBR temperature sensors. A sensor is fixed every 3 m from a depth of 21 m to 90 m.

Some sensors were not working properly, giving incorrect results. These data were discarded from the analysis (section 3.5.1).

The temperature profiles provided by the temperature chain are used to calculate the mixing layer depth (h_m) for the period under study. Therefore, temperature chain allow to have a global vision of the mixing layer depth on a long-term, and will be particularly useful in the statistical analysis.

2.4 Light extinction length scale λ

Thetis is an autonomous profiler measuring vertical temperature, oxygen and chlorophyll data. It can also acquire electrical conductivity, hyperspectral absorption and attenuation (AC-S), backscattering and fluorescence at discrete wavelengths, hyperspectral up and downwelling radiation and PAR radiation (Minaudo et al., 2021). Normally, the Thetis can be used to obtain light extinction length scale λ every 6 hours. However, there are some periods of time where the Thetis is not deployed for maintenance. Thetis measurements were available for the year 2020, but was not for the two first months of 2021. For a given time, a λ value is estimated based on the nearest value and/or values from other year at the same period.

The attenuation coefficient of downwelling irradiance is estimated with equation 2.1 (Mobley, 1994):

$$k_d = -\frac{1}{z_2 - z_1} \ln \frac{I(z_1)}{I(z_2)}, \quad (2.1)$$

where k_d is the attenuation coefficient m^{-1} , z is the depth defined positive upward, $I(z)$ the shortwave radiation at depth z provided by the Thetis. The light extinction length scale is defined as the inverse of the attenuation coefficient:

$$\lambda = k_d^{-1} \quad (2.2)$$

2.5 Short-term data: μ CTD profiler

Diurnal mixing layer can have temperature variation magnitude of $\mathcal{O}(0.01^\circ\text{C})$. Microstructure and turbulence related quantities were made available using a μ CTD (Conductivity & Temperature Depth) profiler allowing to characterize in many ways the water column. Developed by Rockland Scientific International Inc. (RSI), the instrument has a length of 1 m and is equipped with turbulence and water quality sensors located at the front bulkhead. Turbulence properties are measured with two microstructure airfoil shear probes and two fast-response temperature sensors (type FP07) and are sampled at high frequency (512 Hz). It is difficult to take direct measurement of turbulent fluxes in natural systems (Moum, 1996). Turbulent diffusivity is thus estimated by doing measurements of turbulent kinetic energy (TKE) and the temperature variance dissipation rates (Osborn, 1980) following the procedure described

in Piccolroaz et al. (2021). The turbulence quantities (like the turbulent diffusivity κ_T) are averaged over 0.5 m length segments in the post processing. Water temperature sensors (CT), have an accuracy and a resolution of $< 0.01^\circ\text{C}$ and 0.001°C respectively and are sampled at high frequency (512 Hz).

A float is attached to the μCTD and adds buoyancy to the instrument, making it able to operate in upward mode and allows to have high resolution temperature profiles until the very surface. Via post-processing, it is possible to know when the μCTD reaches the surface and filter the data to discard air measurements. Measurement of μCTD are ordered by days. A campaign of measurement is not always starting and ending at the same time of the day, but have similar temporal resolution: each measurement are separated by more or less 10 minutes. In the following work, we consider various μCTD profiles taken between the year 2020 and 2021, with a special focus on a microstructure profile taken on the 18th of january 2021 where a competitive behavior between shortwave radiation and cooling takes place.

3 Methods

A natural phenomenon can be investigated by trying to describe it through mathematical equations (models) that encapsulate the key physical processes. Such models can be more or less complex. By adopting a methodology, going from simple to complex, it is possible to prioritize the driven mechanisms explaining the nature of the phenomenon in question and give a critical explanation of the assumptions considered. A simple model with a good explanation on the assumptions and on the aspects not implemented can help to understand better a physical phenomenon.

3.1 Governing equations

Advection and diffusion are two processes describing the evolution of temperature in a medium. These physical processes can be mathematically modelled by the advection-diffusion equation:

$$\frac{\partial T}{\partial t} + \nabla \cdot (\mathbf{v} T) = \nabla \cdot (D \nabla T) + S, \quad (3.1)$$

where \mathbf{v} (m s^{-1}) is the velocity field, D is the molecular diffusion ($\text{m}^2 \text{s}^{-1}$), T the temperature field and S is a source term.

Considering the vertical transport (1D) equation with solar radiation for the temperature field, the following equation ensue.

$$\frac{\partial T}{\partial t} + \frac{\partial}{\partial z} (\mathbf{v} T) = \frac{\partial}{\partial z} \left(D \frac{\partial T}{\partial z} \right) + \frac{\partial I_r}{\partial z}. \quad (3.2)$$

For simplicity, advection mechanism described by the term $\frac{\partial}{\partial z} (\mathbf{v} T)$ is included in the effective turbulent diffusivity κ_T .

$$\frac{\partial T}{\partial t} = \frac{\partial}{\partial z} \left(\kappa_T \frac{\partial T}{\partial z} \right) + \frac{\partial I_r}{\partial z}, \quad (3.3)$$

where z (m) is the vertical axis coordinate whose origin is at the air-water interface and positive upward. $T(t, z)$ is the temperature field, $I_r = I_0 e^{\frac{z}{\lambda}}$ is a depth-dependent kinematic flux that models the action of solar radiation across the water column based on the Beer-Lambert's law. I_0 denotes the surface radiative kinematic flux due to shortwave radiation at $z = 0$ and is determined from the net shortwave radiation absorbed at the surface water.

To solve equation 3.3, we define Neumann boundary condition at the surface and a Dirichlet boundary conditions at the bottom. Initial condition of the temperature field is set constant, mimicking a fully mixed profile.

$$\begin{cases} \frac{\partial T}{\partial t} = \frac{\partial}{\partial z} \left(\kappa_T \frac{\partial T}{\partial z} \right) + \frac{I_0}{\lambda} e^{\frac{z}{\lambda}} \\ -\kappa_T \frac{\partial T}{\partial z} \Big|_{z=0, t} = Q_0 \\ T \Big|_{z=h_r, t} = T_r, \end{cases} \quad (3.4)$$

Q_0 defines the surface cooling kinematic flux (Kms^{-1}). $T \Big|_{z=h_r, t}$ denotes the temperature at a reference depth h_r , here defined as the spatial bottom boundary of the system. Physical components described in equation 3.4 act on the near-surface layer and are considered responsible for the change of convection regime at a daily timescale. In order to fully determine the temperature profile of the near-surface layer, h_r is associated to the seasonal mixing layer depth h_m , and is defined as the depth where surface convection may take place due to mixing of the unstable region of the temperature profile.

3.1.1 Problem scales

Equation 3.3 can be rewritten into a dimensionless equation. The source term $\frac{I_0}{\lambda} e^{z/\lambda}$ suggests that z can be scaled using λ , such that $z = \tilde{z} \lambda$, where the tilde represents the correspondent dimensionless variable.

Equation 3.4 (assuming that κ_T is constant with depth and time) becomes:

$$\frac{\lambda}{I_0} \frac{\partial T}{\partial t} = \frac{\lambda}{I_0} \frac{\kappa_T}{\lambda^2} \frac{\partial^2 T}{\partial \tilde{z}^2} + e^{\tilde{z}}.$$

In order to have a dimensionless component multiplying $\frac{\partial T^2}{\partial \tilde{z}^2}$, the dimensionless temperature (\tilde{T}) can be defined as $T = \tilde{T} \left(\frac{\lambda I_0}{\kappa_T} \right)$.

$$\frac{\lambda^2}{\kappa_T} \frac{\partial \tilde{T}}{\partial t} = \frac{\partial^2 \tilde{T}}{\partial \tilde{z}^2} + e^{\tilde{z}}.$$

Time t is scaled by λ^2/κ_T .

Scales components can be resumed as follows:

$$\begin{cases} z = \tilde{z} \lambda \\ h_r = \tilde{h}_r \lambda \\ \lambda = \tilde{\lambda} h_r \\ t = \frac{\lambda^2}{\kappa_T} \tilde{t} \\ R = \frac{Q_0}{I_0} \end{cases} \quad (3.5)$$

R is defined as the ratio between surface cooling and radiative heating. Equation 3.6 is the dimensionless version of equation 3.3 considering the scaling presented in 3.5:

$$\frac{\partial \tilde{T}}{\partial \tilde{t}} = \frac{\partial^2 \tilde{T}}{\partial \tilde{z}^2} + e^{\tilde{z}}, \quad (3.6)$$

with the boundary conditions :

$$\begin{cases} -\frac{\partial \tilde{T}}{\partial \tilde{z}} \Big|_{\tilde{z}=0, \tilde{t}} = \frac{Q_0}{I_0} = R \\ \tilde{T} \Big|_{\tilde{z}=\tilde{h}_r, \tilde{t}} = \tilde{T}_r \end{cases} \quad (3.7)$$

where the profile at $t = 0$ is set constant, mimicking a fully mixed temperature profile:

$$\tilde{T} \Big|_{\tilde{z}, \tilde{t}=0} = \tilde{T}_{ref}, \quad (3.8)$$

where $\tilde{T}_{ref} = \frac{\lambda I_0}{\kappa_T} \cdot T_{ref}$, T_{ref} being the reference temperature at $t = 0$. T_{ref} can be estimated depending on the season where the measurement is made.

Convection timescale

Convection is controlled by the timescale τ_{conv} of the forcing mechanism (surface cooling and radiative heat flux),

Bouffard and Wüest (2019) give an estimation on the convective scale velocity w_c based on the buoyancy flux B . By assuming that the effective buoyancy flux has the same order of magnitude than the surface buoyancy flux (B_0), the convective scale velocity can be approximated using

equation 3.9.

$$w_c = (B_0 h)^{1/3}. \quad (3.9)$$

Equation 3.10 is used to estimate B_0 based on the surface heat flux H_0 (Wm^{-2}):

$$B_0 = \frac{g}{\rho} \left(\frac{\alpha}{c_p} H_0 \right), \quad (3.10)$$

with the water specific heat capacity c_p ($\text{Jkg}^{-1} \text{K}^{-1}$), a reference water density ρ (kgm^{-3}), α is the thermal expansion coefficient (K^{-1}) and have an order of magnitude of 10^{-5}K^{-1} . Equation 3.10 neglects salinity and suspended particles.

We can thus have an estimation of the convection timescale:

$$\tau_{conv} = \frac{h}{w_c}. \quad (3.11)$$

To have an order of magnitude on the convection timescale, we base our estimation on reasonable values taken from a winter day by choosing $h \approx 10 \text{ m}$, $H_0 \approx 100 \text{ Wm}^{-2}$. The resulting convection timescale is approximately 30 min, which corresponds to what have been found in Imberger (1985).

Surface cooling and solar radiation timescale

Kinematic fluxes entering or exiting the system are described through these two equations:

$$\kappa_T \frac{\partial T}{\partial z} = Q_0, \quad (3.12)$$

$$I = I_0 e^{z/\lambda}. \quad (3.13)$$

Imagining that both kinematic fluxes are responsible of the change of temperature ΔT , the correspondent timescales can be approximated by:

$$\tau_C = \frac{\Delta T}{Q_0} h, \quad (3.14)$$

$$\tau_H = \frac{\Delta T}{\langle I \rangle_h} h, \quad (3.15)$$

with $\langle I \rangle_h$ being the progressive averaging of the solar radiation penetrating the water column described in 3.16:

$$\langle I \rangle_h = \frac{1}{h} \int_{z=-h}^{z=0} I(z) dz = \frac{1}{h} \int_{z=-h}^{z=0} I_0 e^{z/\lambda} dz = \frac{I_0 \lambda}{h} (1 - e^{-h/\lambda}). \quad (3.16)$$

Then the ratio of the two timescales can be calculated as:

$$\frac{\tau_H}{\tau_C} = \frac{Q_0 h}{I_0 \lambda} \frac{1}{1 - e^{-h/\lambda}} = R \frac{h}{\lambda} \frac{1}{1 - e^{-h/\lambda}}. \quad (3.17)$$

Kinematic flux timescale order of magnitude

ΔT can have an order of magnitude of $\mathcal{O}(10^{-2} - 10^{-1})$ within a day considering the diurnal mixing depth. Surface cooling and solar radiation have an order of magnitude of $\mathcal{O}(10^{-5})$ (K.m.s^{-1}). h and λ have a magnitude of approximately $\mathcal{O}(10)\text{m}$.

With τ_C being the cooling timescale and τ_H the radiative heating timescale:

$$\tau_C = \frac{\Delta T}{Q_0} h = \frac{0.1}{1 \cdot 10^{-5}} \cdot 10 \approx 1 \cdot 10^5 \text{ s} \approx 27 \text{ h}, \quad (3.18)$$

$$\langle I \rangle_h = \frac{I_0 \lambda}{h} (1 - e^{-h/\lambda} - 1) = \frac{1 \cdot 10^{-5} 10}{10} (1 - e^{-10/10}) \approx 6 \cdot 10^{-6} \text{ K.m.s}^{-1}, \quad (3.19)$$

$$\tau_H = \frac{\Delta T}{\langle I \rangle_h} h = \frac{0.1}{6 \cdot 10^{-6}} 10 \approx 44 h. \quad (3.20)$$

To rise the temperature by 0.1°C of a water column of depth h , the radiative heating by solar radiation and surface cooling would have an order of magnitude of 10^1 h .

3.2 Steady state solution

We first investigate the joint action of surface cooling and radiative heating by looking at the steady state solution of equation 3.4. Solving this problem at steady state condition can give a good idea of how the temperature profile should behave in function of I_0 and Q_0 . At steady

state, i.e. $\frac{\partial T}{\partial t} = 0$, the heat equation 3.4 reduces to:

$$\kappa_T \frac{\partial^2 T}{\partial z^2} = -\frac{I_0}{\lambda} e^{z/\lambda}. \quad (3.21)$$

Equation 3.21 is a second order ordinary differential equation that can be expressed in dimensionless terms:

$$\begin{cases} \frac{\partial^2 \tilde{T}}{\partial \tilde{z}^2} = -e^{\tilde{z}} \\ \frac{\partial \tilde{T}}{\partial \tilde{z}} \Big|_{\tilde{z}=0} = -\frac{Q_0}{I_0} = -R \\ \tilde{T} \Big|_{\tilde{z}=-\tilde{h}_r} = \tilde{T}_r \end{cases} \quad (3.22)$$

$$\frac{\partial \tilde{T}(\tilde{z})}{\partial \tilde{z}} = -e^{\tilde{z}} + C_1, \quad (3.23)$$

$$T(\tilde{z}) = -e^{\tilde{z}} + C_1 \tilde{z} + C_2, \quad (3.24)$$

where C_1 and C_2 are constants depending on boundary conditions defined in equation 3.22.

Based on the top Neumann boundary condition:

$$C_1 = 1 - R,$$

C_2 can also be obtained based on the bottom Dirichlet boundary condition:

$$C_2 = \tilde{T}_r + e^{-\tilde{h}_r} + \tilde{h}_r C_1.$$

The final dimensionless equation for steady state conditions is:

$$\tilde{T}(\tilde{z}) = -e^{\tilde{z}} + (1 - R)(\tilde{z} + \tilde{h}_r) + \tilde{T}_r + e^{-\tilde{h}_r}. \quad (3.25)$$

3.2.1 Compensation depth

Since the system undergoes surface cooling, cold parcels form at the near-surface layer and sinks due to gravity, forming an unstable layer. Convective plumes are created, sink and penetrate into a stable (enhanced by shortwave radiation) layer below (Soloviev and Lukas, 2014).

Under the assumption that those two kinematic fluxes are the main component driving stability of the water column, the compensation depth (h_c or in dimensionless terms $\tilde{h}_c = h_c/\lambda$) is defined as the depth where the surface cooling kinematic flux is balanced by shortwave radiation. By defining this specific depth, it is possible to have a better understanding of where is the region where these convective plumes are created based on injection of shortwave radiation and surface cooling kinematic fluxes. In mathematical term, this means that the total kinematic flux at the compensation depth is equal to zero: $Q|_{z=-h_c} = 0 \text{ K m s}^{-1}$. If one integrates equation 3.21 from the compensation depth h_c to the surface:

$$\int_{-h_c}^0 \kappa_\tau \frac{\partial^2 T}{\partial z^2} dz = \int_{-h_c}^0 -\frac{I_0}{\lambda} e^{z/\lambda} dz, \quad (3.26)$$

from the Neumann boundary conditions at $z = 0$ described in equation 3.4:

$$\kappa_\tau \frac{\partial T}{\partial z} \Big|_{z=0} - \kappa_\tau \frac{\partial T}{\partial z} \Big|_{z=-h_c} = -I_0 \left(1 - e^{-h_c/\lambda}\right), \quad (3.27)$$

as the compensation depth is defined as the depth where the kinematic flux equals zero, we simplify as following

$$-Q_0 - Q|_{z=-h_c} = -I_0 \left(1 - e^{-h_c/\lambda}\right), \quad (3.28)$$

by integrating dimensionless quantities defined in 3.5 and putting forward the R ratio

$$-R = -1 + e^{-\tilde{h}_c}, \quad (3.29)$$

$$\tilde{h}_c = -\ln(1 - R), \quad (3.30)$$

From the logarithmic function behavior, the dimensionless compensation depth is therefore defined if $R < 1$ and will have no physical meaning if $R < 0$. This expression is therefore valid for $R \in]0, 1[$, meaning that the lake is cooling and $I_0 > Q_0$.

3.2.2 Analytical Mixing depth at steady state conditions

The analytical convective mixing depth is here defined as the depth where surface convection takes place in presence of shortwave radiation and surface cooling. It is identified by computing a progressive averaging (mimicking convective mixing) of the steady state temperature profile, moving from the surface downwards (\tilde{T}_{avg}):

$$\tilde{T}_{avg} = \frac{1}{\tilde{z}} \int_{\tilde{z}}^0 \tilde{T} d\tilde{z}, \quad (3.31)$$

with equation 3.25, the integral is developed as follow :

$$\frac{1}{\tilde{z}} \int_{\tilde{z}}^0 \tilde{T} d\tilde{z} = \tilde{T}_r \tilde{z} + \tilde{z} e^{-\tilde{h}_r} - e^{\tilde{z}} + \left(\frac{\tilde{z}^2}{2} + \tilde{h}_r \tilde{z} \right) (1 - R) + 1. \quad (3.32)$$

Thus, the convective mixing depth is identified by finding out the depth at which \tilde{T}_{avg} intersects the steady state temperature profile \tilde{T} (3.2)

$$\tilde{T}_{avg} = \tilde{T}, \quad (3.33)$$

$$\tilde{T}_r + e^{-\tilde{h}_r} - \frac{1}{\tilde{z}} e^{\tilde{z}} + \left(\frac{\tilde{z}}{2} + \tilde{h}_r \right) (1 - R) + \frac{1}{\tilde{z}} = \tilde{T}_r + e^{-\tilde{h}_r} - e^{\tilde{z}} + (1 - R) (\tilde{z} + \tilde{h}_m), \quad (3.34)$$

$$e^{\tilde{z}} + \frac{\tilde{z}^2}{2} (1 - R) - 1 - \tilde{z} e^{\tilde{z}} = 0. \quad (3.35)$$

Equation 3.35 can be solved numerically. One root is always $\tilde{z} = 0$. For the other roots, we have :

$$\begin{cases} \tilde{z} > 0 \text{ for } R < 0 \\ \tilde{z} \in \mathbb{C} \text{ for } R > 1 \\ \tilde{z} < 0 \text{ for } R \in]0, 1[\end{cases} \quad (3.36)$$

z is defined positive upward, therefore a positive root has no meaning in the case studied (surface cooling). A complex root has no physical meaning in this context. Similarly to the compensation depth, the convective mixing depth is defined for $R \in]0, 1[$. Note that the roots do not depend on \tilde{T}_r .

Finally, the mixed stable profile \tilde{T}_{mix} is obtained by averaging the steady state temperature profile from surface down to the convective mixing depth (h_m). Below the convective mixing depth, the profile is equal to the steady state solution:

$$\tilde{T}_{mix} = \begin{cases} \langle \tilde{T} \rangle & \tilde{z} \geq -\tilde{h}_m \\ \tilde{T}_{mix} & \tilde{z} < -\tilde{h}_m \end{cases} \quad (3.37)$$

3.3 Numerical modelling

The steady state solution has the particularity to be easily interpreted analytically, but is not well adapted to reproduce the dynamism of the phenomena. On one hand, the heat equation may take time to reach steady state. On the other hand, convection due to the formation of denser water parcel also takes time to mix. To overcome the limitations of the steady state solution, and more specially to integrate the possible evolution of the temperature profile with time, a numerical model for the 1D heat equation is introduced in this section. To assess the importance of mixing phenomena, further improvement in the model will consider mixing events at different recurrences.

3.3.1 Simple 1D implicit model

Many numerical schemes can be used to simulate the physical processes we are interested here. Some of them are more complex to implement than others. The implicit method is favored among others because it is unconditionally stable, but have the down side to be slower (Olsen-Kettle, 2011).

Implicit methods find a solution by solving the discretized heat equation involving both the current state (t_k) and the later one (t_{k+1}), making the system more stable by integrating a strong dependence between different timesteps. Let's consider the temperature $T(z, t)$ with $-h_r \leq z \leq 0$ and $0 \leq t \leq T$. h_r being the maximum depth under the assumption that at this depth, temperature remains constant. Δz and Δt are fixed parameters, m is the number of layers and n is the number of timestep. At a specific time k and at the layer j , we have : $t_k = k \Delta t$, $0 \leq k \leq m$ and $z_j = j \Delta z$, $0 \leq j \leq n + 1$

Temperature derivatives are discretized considering time k and layer j (κ_r is considered constant with depth and time):

$$\frac{\partial T}{\partial t} \rightarrow T_t(t = k + 1) \approx \frac{T_j^{k+1} - T_j^k}{\Delta t}, \quad (3.38)$$

$$\frac{\partial^2 T}{\partial z^2} \rightarrow T_{zz}(z = j, t = k + 1) \approx \frac{T_{j-1}^{k+1} - 2T_j^{k+1} + T_{j+1}^{k+1}}{\Delta z^2}. \quad (3.39)$$

Equation 3.3 can be rewritten in its discrete form:

$$\frac{T_j^{k+1} - T_j^k}{\Delta t} = \kappa_r \frac{T_{j-1}^{k+1} - 2T_j^{k+1} + T_{j+1}^{k+1}}{\Delta z^2} + f_j^k, \quad (3.40)$$

$$T_j^k + f_j^k \Delta t = T_j^{k+1} - \frac{\kappa_T \Delta t}{\Delta z^2} \left(T_{j-1}^{k+1} - 2T_j^{k+1} + T_{j+1}^{k+1} \right), \quad (3.41)$$

$f_j^k = \frac{I_0^k}{\lambda} e^{\frac{j}{\lambda}}$ describes the solar radiation at each point j at time k .

By setting $r = \frac{\Delta t}{\Delta z^2}$, and rearranging equation 3.41 becomes:

$$T_j^k + f_j^k \Delta t = -r \kappa_T T_{j-1}^{k+1} + (1 + 2\kappa_T r) T_j^{k+1} - r \kappa_T T_{j+1}^{k+1}. \quad (3.42)$$

We have Neumann boundary condition at the top :

$$\left. \frac{\partial T}{\partial z} \right|_{z=0} = -\frac{Q_0}{\kappa_T} = -\frac{T_0 - T_{-1}}{\Delta z} \iff T_{-1} = -\frac{Q_0}{\kappa_T} \Delta z + T_0, \quad (3.43)$$

with T_{-1} defined as a ghost point (point above the surface).

Going back to equation 3.42

$$T_0^k + f_0^k \Delta t = -r \kappa_T T_{-1}^{k+1} + (1 + 2\kappa_T r) T_0^{k+1} - r \kappa_T T_1^{k+1},$$

substituting T_{-1}^{k+1} :

$$T_0^k + f_0^k \Delta t = -r \kappa_T \left(-\frac{Q_0}{\kappa_T} \Delta z + T_0^{k+1} \right) + (1 + 2\kappa_T r) T_0^{k+1} - r \kappa_T T_1^{k+1},$$

$$(1 + r \kappa_T) T_0^{k+1} - r \kappa_T T_1^{k+1} = T_0^k - Q_0 \frac{\Delta t}{\Delta z} + f_0^k \Delta t. \quad (3.44)$$

Equation 3.41, given the boundary exception expressed in equation 3.44 can be described for each temporal and spatial step by the following system :

$$\begin{bmatrix} 1 + r \kappa_T & -r \kappa_T & 0 & \dots & \dots & 0 \\ 0 & 1 + 2r \kappa_T & -r \kappa_T & 0 & \dots & \vdots \\ \vdots & -r \kappa_T & \ddots & \ddots & \dots & \vdots \\ \vdots & \ddots & \ddots & \ddots & \ddots & \vdots \\ 0 & \dots & \dots & -r \kappa_T & 1 + 2r \kappa_T & 0 \end{bmatrix} \begin{bmatrix} T_0^{k+1} \\ \vdots \\ \vdots \\ \vdots \\ T_{m-1}^{k+1} \end{bmatrix} = \begin{bmatrix} T_0^k \\ \vdots \\ \vdots \\ \vdots \\ T_{m-1}^k \end{bmatrix} + \begin{bmatrix} -Q_0 \frac{\Delta t}{\Delta z} + f_0^k \Delta t \\ f_1^k \Delta t \\ \vdots \\ \vdots \\ r \kappa_T T_{z=m}^{k=0} + f_{m-1}^k \Delta t \end{bmatrix} \quad (3.45)$$

Note that temperature is calculated from $m = 0$ to $m - 1$. To respect Dirichlet boundary conditions, $T_m^k = T_m^{k=0} = T_{ref}$ is set.

At time $k=0$, the temperature profile is set constant : $T_{0,1,2,..,m}^{k=0} = T_{ref}$

This system can be solved, giving a profile of temperature at each timestep by using the Thomas algorithm proposing an efficient way of solving tridiagonal matrix systems (Thomas, 1949). Note that the initial temperature profile is set as the bottom temperature but can obviously be different.

3.3.2 Time & spatially dependent parameters

Diffusivity, solar radiation are in reality spatially and time dependent and surface cooling is time dependent (surface flux).

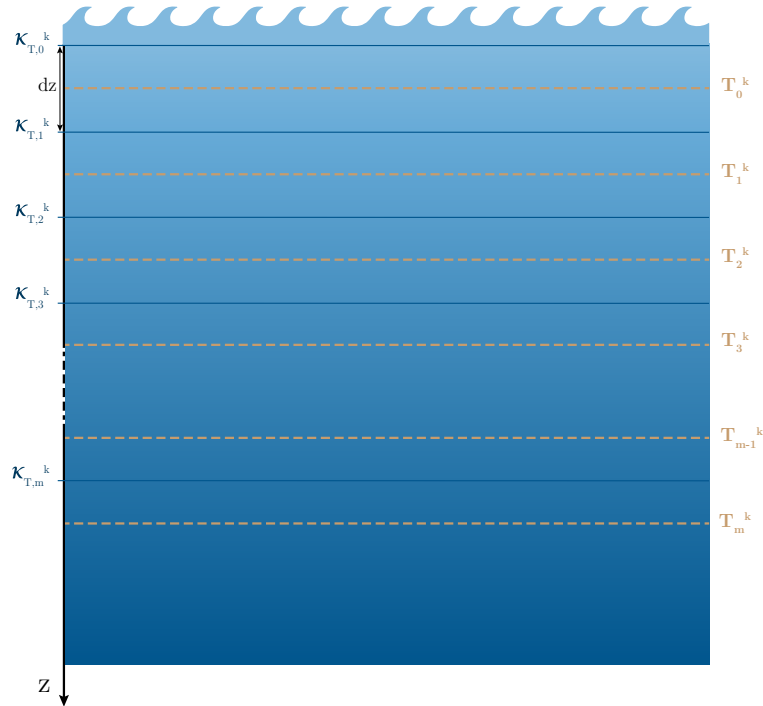


Figure 3.1 – Model grid for discretization of the heat equation at a time t .

κ_T is defined at the edges, whereas T is defined at the center of each layers. In the frame of this work, measurements taken with the μCTD profiler are providing values of diffusivity at each time and depth. μCTD measurements are therefore used to give an additional inputs to the numerical model, but also to assess the potential difference between the modelled and actual temperature profile. This way, the numerical model can be used to replicate a

specific day where microstructure data are available. Temperature profiles are updated and stored at each timestep Δt . Each μ CTD profiles were taken with an interval $\Delta t_2 \approx 10$ min. The following system has now varying parameters updated every 10 min in the implicit loop ($\kappa_T = \kappa_T(z, t)$, $Q_0 = Q_0(t)$, $f = f(z, t)$).

$$\begin{aligned}
 & \begin{bmatrix} 1 + r\kappa_{T,0}^k & -r\kappa_{T,0}^k & 0 & \dots & \dots & 0 \\ 0 & 1 + r(\kappa_{T,0}^k + \kappa_{T,1}^k) & -r\kappa_{T,1}^k & 0 & \dots & \vdots \\ \vdots & -r\kappa_{T,0}^k & \ddots & \ddots & \dots & \vdots \\ \vdots & \ddots & \ddots & \ddots & \ddots & \vdots \\ 0 & \dots & \dots & -r\kappa_{T,m-1}^k & 1 + r(\kappa_{T,m-1}^k + \kappa_{T,m}^k) & 0 \end{bmatrix} \begin{bmatrix} T_0^{k+1} \\ \vdots \\ \vdots \\ \vdots \\ T_{m-1}^{k+1} \end{bmatrix} = \begin{bmatrix} T_0^k \\ \vdots \\ \vdots \\ \vdots \\ T_{m-1}^k \end{bmatrix} \\
 & + \begin{bmatrix} -Q_0 \frac{\Delta t}{\Delta z} + f_0^k \Delta t \\ f_1^k \Delta t \\ \vdots \\ \vdots \\ r\kappa_{T,m} T_{z=m}^{k=0} + f_{m-1}^k \Delta t \end{bmatrix}
 \end{aligned}$$

Similarly, the Dirichlet boundary condition is set at the bottom, but updated at each 10 min timestep : $T_m^k = T_{ref, \mu CTD}$

3.3.3 Empirical Mixing depth algorithm

The numerical model may produce unstable systems where mixing should happen. Unfortunately, no analytical expression allow to estimate the mixing layer depth. To reproduce convective mixing in the unstable regions an algorithm based on the relative decrease in temperature with depth is implemented. As suggested by figure 3.2, this algorithm is based on the same idea presented in section 3.2.2. The average temperature is done iteratively from top to bottom. When the iterative average temperature meets the actual temperature, the algorithm stops and the depth is defined as the mixing depth (h_m). The mixed stable profile \tilde{T}_{mix} is obtained by averaging the measured temperature profile from surface down to the convective mixing depth. Below the convective mixing depth, the profile is defined as there is no mixing happening.

$$\tilde{T}_{mix} = \begin{cases} \langle \tilde{T} \rangle & \tilde{z} \geq -\tilde{h}_m \\ \tilde{T} & \tilde{z} < -\tilde{h}_m \end{cases} \quad (3.46)$$

Figure 3.2 – Click on the figure to animate it. This figure shows the mixing layer algorithm. The blue curve is the temperature profile, T is the actual temperature for a given temperature, \tilde{T} is the mean temperature from the surface to the reference depth. The vertical line on the right show the respective position of T with \tilde{T} . When the two points crosses each other, the algorithm stop and the depth is recorded as the mixing depth.

Based on the convection timescale, mixing has been implemented in the numerical model by applying equation 3.46 every half an hour (corresponding to convection timescale τ_{conv}). To assess the importance and the effect of mixing, two more situation where investigated, the numerical model is therefore implemented considering three cases:

- application of the mixing algorithm every ≈ 30 min
- application of the mixing algorithm at every model's timestep $\Delta t = 1$ min
- without any mixing.

3.4 Model and μ CTD temperature profiles comparison

The model produces profiles at each timestep Δt . Long-term data information are provided for each profile, updating forcing parameters with a 10 min resolution. Parameters like diffusivity

κ_T and kinematic fluxes, are therefore integrated and thus kept constant in time for a 10 min period.

To facilitate the visualization of the high frequency microstructure data, temperature profiles are smoothed using a Savitzky-Golay filter (Savitzky, 1964). The parameters input for this filter are the window size and the polynomial order. The polynomial order is set as $n = 3$. The window size depends on the number of data. For example, for the high frequency data (512 Hz), a window size of 300 points will smooth most of the effect of turbulence and the error variability of the μ CTD,

To assess the quality of the implicit model, measurements from the 18th of January 2021 are given as input to the model. This day is chosen over the others in particular because negligible wind speed was recorded and had a large temporal coverage. The model and the μ CTD temperature profile are displayed jointly by choosing the closer modelled profile corresponding to the profile measurement.

3.4.1 Model skill metric (MSM)

The model skill metric (MSM) is used to assess the model performance (Willmott1981). It is defined as following:

$$MSM = 1 - \frac{\sum |T_{mod} - T_{obs}|^2}{\sum \left(\left| T_{mod} - \bar{T}_{obs} \right| + \left| T_{obs} - \bar{T}_{obs} \right| \right)^2}, \quad (3.47)$$

where T_{mod} is the modeled temperature profile, T_{obs} the observed temperature profile and its mean \bar{T}_{obs} . The range for the MSM values is between 0 and 1, a MSM value close to 1 imply better model performance.

3.5 Statistical Analysis

The R ratio is defined in a way that if R is high, surface cooling prevails over shortwave radiation leading to instability and mixing, if $R < 0$ heat is added to the system thereby favouring stratification. In the case of $R \approx 1 \pm \delta$, δ being an increment that will be evaluated later, shortwave radiation and surface cooling are rivalry influencing the near-surface layer.

The steady state solution is considering the system at its equilibrium and allows to define in a more categorical way three physical states depending on the R range: fully mixed ($R < 0$), transition ($R \in [0, 1]$), and stratified ($R > 1$) Having in mind the different conditions on when the different states should happen, it is possible to give a look at the continuous data measured in the platform, to have an idea of the persistency of each states during the year.

Note that thresholds of other parameters than R used in this statistical analysis are derived from observations, i.e a diurnal mixing depth less than 5 m is considered stratified. The idea

is to have an estimation of the time during the year in which our hypothesis on the state is fulfilled. As this phenomena depends on different parameters, it is necessary to apply each conditions on each 10 min measurement.

Those conditions are resumed in table 3.1, .

Threshold conditions	Wind (m s^{-1})	h_m (m)	R
Transition	<2	>5	[0; 1]
Fully mixed	>0	>5	>1
Stratified	<2	<3	$[-\infty; 0]$

Table 3.1 – Condition threshold for different convection regimes at steady state.

As we investigate convective regimes under no or negligible conditions, a condition on wind is set as lower than 2 m s^{-1} .

Three different states are described in table 3.1. Because we are interested in a system where convection happens and where shortwave radiation plays a significant role, we will be interested mainly on the transition conditions (corresponding to the transition regime).

3.5.1 Mixing layer depth estimation with temperature chain

Temperature chain data were imported from Datalakes from April 2020 to April 2021. These data give a general view of the mixing depth with a 10 min time resolution.

One of the condition given in table 3.1 for the transition regime to happen is to have a mixing layer. If the temperature chain shows a stratified water column, this period is discarded from the statistical analysis.

During some period of time, some sensors were not working, or giving strange results. Those sensors were manually removed and filtered. Moreover, if a profile of temperature have more than half of its sensors not working, this profile were not taken into account. Once filtered, data without values were linearly interpolated to give a continuous temperature profile (following the space resolution described in section 2.3).

As well described in Thomson and Fine (2003), estimation of mixing depth in ocean varies, in most cases, between a relative density difference of $\Delta\rho \in (0.01 - 0.03 \text{ kg m}^{-3})$.

Conversion of density to temperature assuming no salinity is based on the following formula:

$$\frac{\Delta\rho}{\rho} = -\alpha(T) \cdot \Delta T. \quad (3.48)$$

From Bouffard and Wüest, (2018), the thermal expansion coefficient can be approximated:

$$\alpha(T) = 10^{-6} (-65.4891 + 17.12544 T - 0.178155 T^2). \quad (3.49)$$

As it is assumed no salinity difference with depth in Lake Geneva, and taking into account the low space resolution for the temperature chain, estimation of the mixing depth is based on a temperature difference between $z = 0$ and $z = -h_m$ of $\Delta T = 0.02^\circ C$ and is consistent with what Gray et al. (2020) found. This estimation of the mixing layer depth is favoured over the one described in section 3.3.3 because of its low computational cost, and because it is adapted to the space resolution of the temperature chain data.

3.6 Cloud cover

In datalakes, daily cloud cover is computed according to the Woolway et al. (2015) procedure. The Zenith angle is necessary for the procedure, and is calculated via the pysolar library, specialized in precise ephemeris calculations or simulation of the irradiation of any point on earth by the sun (Reda and Andreas, 2008). Empirical equations computing heat fluxes uses daily cloud cover fraction (ccf) to provide a 10 min resolution as an output.

Absorbed shortwave radiation, absorbed and emitted longwave radiation are calculated according to the procedure described by Fink et al. (2014). Due to the scattering mechanisms, H_{SW} is affected by the presence of clouds.

$$H_{SW} = G F_{dir} (1 - A_{dir}) + G F_{diff} (1 - A_{diff}), \quad (3.50)$$

with

$$F_{dir} = (1 - ccf) [(1 - ccf) + 0.5 ccf]^{-1}, \quad (3.51)$$

$$F_{diff} = (0.5 ccf) [(1 - ccf) + 0.5 ccf]^{-1} \quad (3.52)$$

where G is the global radiation ($W m^{-2}$), ccf (-) is the cloud cover fraction in non-dimensional units from 0 (clear sky) to 1 (complete cover). F_{dir} and F_{diff} the direct and the diffuse shortwave radiation respectively, A_{diff} is the albedo of diffusive shortwave radiation, approximately constant (≈ 0.066), and A_{dir} is retrieved using the "Grishchenko albedo" (Grishchenko, 1959).

In our case, G is actually the measured downward solar radiation and is therefore indirectly influenced by clouds.

4 Results

4.1 Steady state

4.1.1 Building intuition

The steady state solution derived from equation 3.25 enables to understand, based on one parameter, how the convective regimes would possibly evolve on a daily timescale. Figure 4.1 provides this intuitive thinking and tries to replicate each state depending on the parameter R .

It is considered that heat fluxes are the main components responsible for the shape of the temperature profile at steady state. To get how the R ratio is changing on a daily timescale, we can give a physical interpretation on the temperature profile based on the variation of surface cooling and radiative heating. The resulting temperature profile based on the R ratio is displayed with a black curve, and with a dashed grey line if we consider the stable mixed temperature profile as explained in equation 3.37.

Here, it is considered that I_0 is null during night time. At night, the R ratio is therefore maximum ($R \rightarrow \infty$) resulting in a perfectly mixed profile as shown with the stable temperature profile in dashed grey. When the sun rises, I_0 increases slowly while Q_0 is still high, R would progressively approach one. while shortwave radiation increases, the initially mixed temperature profile is subject to progressive heating in particular at the near-surface, resulting in an increase of temperature at the surface and at the bottom. At midday, I_0 is maximum, R would be between 0 and 1, eventually evolving to approach 0. The resulting steady state profile would be balanced; surface cooling would mix the water column until it reaches the calculated mixing depth. As shortwave radiation starts to be preponderant in the system, also warming the air temperature, hot water parcels are also forming at the surface due to surface heating (atmosphere transfers heat to the surface lake waters), making the steady state temperature profile even more stable (R is close to 0 or negative). When the sun sets, shortwave radiation would quickly decrease to reach 0. The resulted R ratio would very quickly change its value from $-\infty$ to ∞ , considering that the air temperature would rapidly become colder than the surface water.

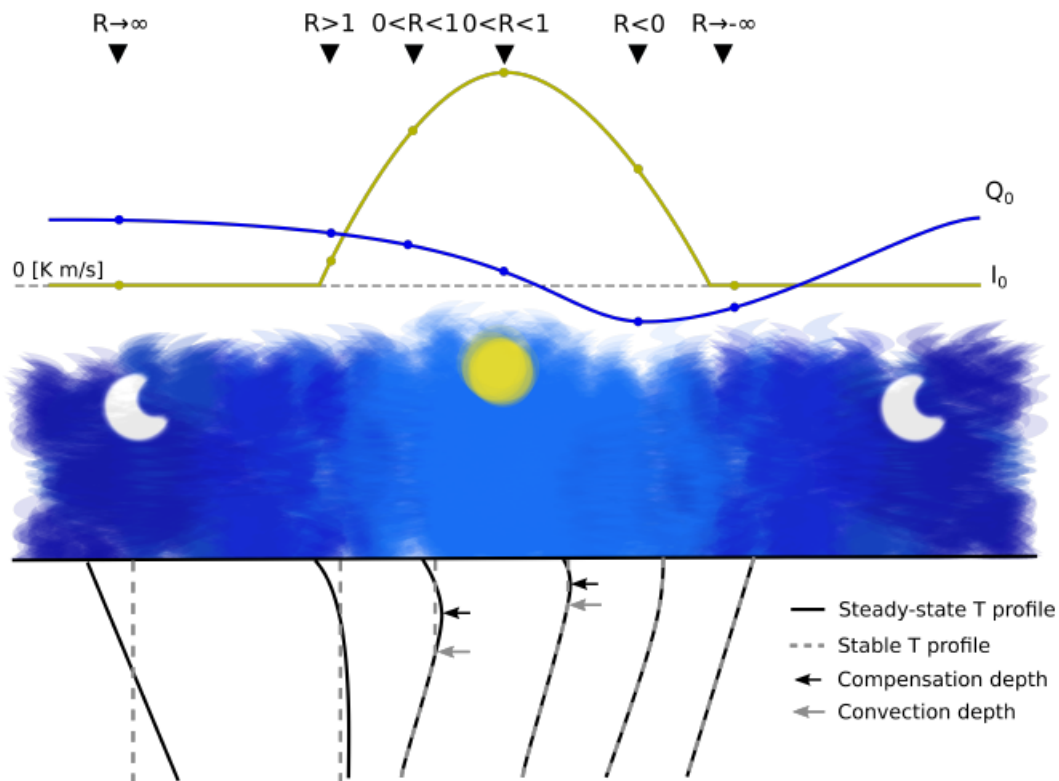


Figure 4.1 – Schematic of the shortwave radiation and surface cooling respective importance in a day. The parameter R is the ratio of the kinematic surface heat flux Q_0 to the surface radiative flux I_0 .

4.1.2 Steady state model

Figure 4.2 shows the effect of a changing R ratio (from -1 to 2) affecting the calculated mixing, compensation depth and the resulting steady state temperature profiles (mixed and ideal).

R ratio

Figure 4.2 a) shows unstable profiles when $R > 1$. Upper denser water will mix within the mixing layer in reality. This mixing process is replicated in figure 4.2 b) considering the stable mixed profile.

Under a pure warming regime ($R < 0$: red region), the steady state model shows strictly stratified profile. The system is warming at the surface ($Q_0 < 0$) and at each depth due to shortwave radiation. Under a pure cooling regime ($R > 1$ blue region), there is a net surface cooling dominating the system, making the profile strictly cooling the more we are at the surface and the stable mixed profile \tilde{T}_{mix} is entirely mixing. When $R \in [0, 1]$, the regime is defined as transitional and the profile starts to show a competition between radiative heating and surface cooling. A transition regime denominates the result of balanced conditions (R between 0 and 1) producing a specific temperature profile shape where both surface cooling and radiative heating have their signature at the surface and along the water column respectively. R is thus a principal component in the characterization of the state system at steady state.

The two black lines, corresponding to the generated profile with a R ratio of 0 and 1 corresponds to the boundary of the transition regime; analytical compensation (equation 3.30) and mixing depth (equation 3.35) can be calculated within that range.

A R ratio between 0 and 1 is of particular interest. The radiative heat flux can have a significant enough influence on the water column to stabilize it. In parallel, surface cooling will still happen at the surface, making the system becoming gravitationally unstable. Convective plumes should take place over the compensation depth (dashed black line) but in fact penetrates deeper, reaching the calculated mixing layer depth (equation 3.35).

Figure 4.2 c) shows the steady state solution \tilde{T} (filled black line), the progressive average temperature profile \tilde{T}_{avg} (red line) and the mixed and stable temperature profile \tilde{T}_{mix} (grey dashed line). As explained in section 3.35, we are searching when $\tilde{T} = \tilde{T}_{avg}$. The red line (\tilde{T}_{avg}) is crossing the modelled steady state profiles at a different depth depending on R . The depth at which the red and black line crosses is the mixing depth corresponding to the analytical mixing depth defined in equation 3.35. If R is close to zero, the mixing depth is at the very surface. If R is closer to one, the mixing depth is situated deeper in the water column.

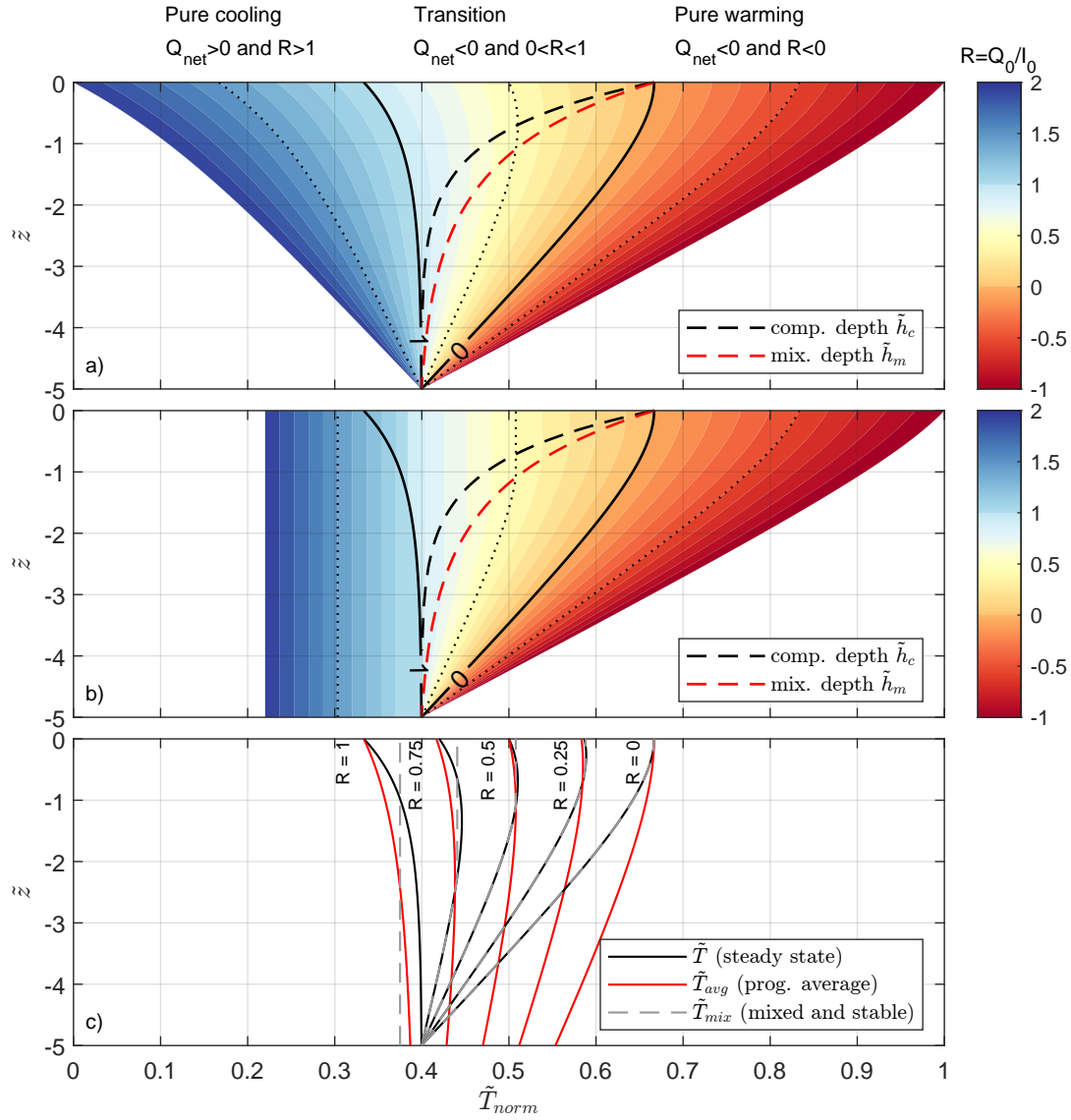


Figure 4.2 – Temperature profiles across different regimes: a) steady state solution \tilde{T} (eq. 3.25), b) stable mixed profile \tilde{T}_{mix} (eq. 3.37), and c) the above profiles compared with the progressively averaged profile \tilde{T}_{avg} (eq. 3.31). \tilde{T}_{norm} is the normalized non dimensional temperature \tilde{T} varying between 0 and 1 (for plotting purposes). The 2 filled black lines in a) and b) is the resulting steady state solution for $R = 0$ and $R = 1$. The black and red dashed line in a) and b) are the compensation depth \tilde{h}_c and mixing depth \tilde{h}_m .

Depth scale

The calculated mixing and compensation depth both decrease by increasing R . Compensation depth is strictly smaller than the mixing depth. Both depth increase exponentially when R approaches 1. The asymptotic behavior is reached when $Q_0 \approx I_0$ and may happen recurrently in one day as described in figure 4.1. Therefore, depth scales are very influenced by the R ratio. A small increase of shortwave radiation with an already low R can make the mixing depth decrease at a higher rate than with an initial R closer to one.

4.2 Timescales

The ratio of the cooling and heating timescales, τ_C and τ_H respectively, is shown in terms of the ratios R and h/λ in figure 4.3.

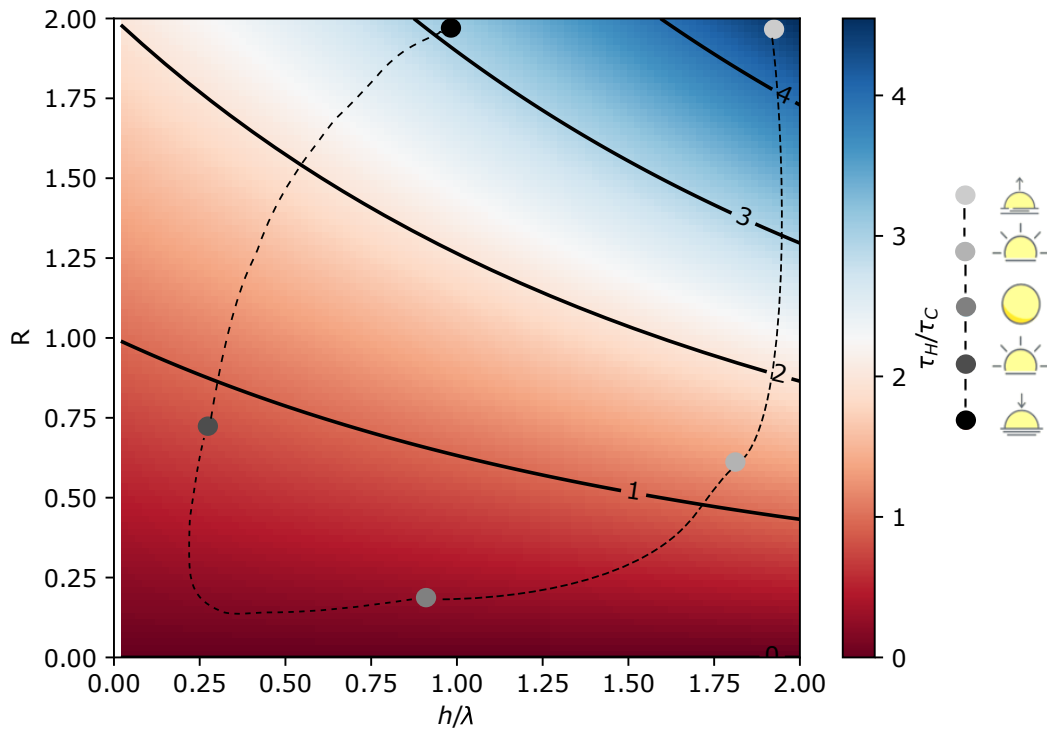


Figure 4.3 – Heat timescales. τ_H/τ_C represent the ratio of the two timescales corresponding to shortwave radiation (τ_H) and surface cooling (τ_C). h is the reference depth, here represented as the mixing depth. λ is the light extinction length scale. The blue line with the points switching from grey to black gives an idea of how the system is changing within a day.

The R ratio varies between 0 and 2, but can reach much higher value within one day ($I_0 \rightarrow 0$ at

the beginning/end of the day). It is considered that the reference depth is the diurnal mixing depth and may therefore vary within a day. For simplicity, light extinction length scale λ is fixed and it is more dependent on seasonality or between different lakes. Considering that the diurnal mixing depth varies from 0 to 10 m and with λ about 5 m for lake Geneva, the h/λ ratio varies between 0 and 2.

A value of ratio $\tau_H/\tau_C > 1$ means that radiative heating will take more time to rise the mean temperature of a water column than surface cooling decreasing it.

From a general perspective, a value of R greater than 1 implies that the effect of surface cooling acts faster compared to radiative heating for any h/λ ($\tau_H/\tau_C > 1$).

Fixing R to 2, an increase in the parameter h will make the effect of radiative heating slower. By fixing h/λ to 2, a decrease of R makes the ratio τ_H/τ_C lower. If R is lower than 0.5 ($I_0 = 2 Q_0$) the effect of radiative heating will act faster than the effect of surface cooling. If the lake is fully stratified (fixing $h/\lambda \approx 0$), increasing shortwave radiation will also make the timescale ratio decrease. The effect of shortwave radiation acts faster than surface cooling with $R < 1$ ($I_0 = Q_0$). Overall, increasing R , the ratio of the two timescales will increase. With a high ratio h/λ , the ratio τ_H/τ_C will be more sensitive to an increase of R than with a low h/λ . In general, an increase of the diurnal mixing depth will increase the timescale ratio τ_H/τ_C .

It is also possible to give a temporal interpretation for this figure, here represented by the points going from light grey to black. The black dashed line correspond to the path of a typical day. In the morning, R is large (I_0 is still low), h/λ is maximum (mixed), the timescale ratio is higher than 1, meaning that effect of surface cooling is quicker than the one of radiative heating.

At midday, the lake is stratified (low h/λ), R is lower or close to 1 (I_0 increases), resulting in a low timescale ratio: radiative heating effect is faster than surface cooling. Thus radiative heating is not only the dominant factor when R is lower than one but also the fastest process compared to surface cooling.

When the sun sets, shortwave radiation decreases quickly, R increases, and surface cooling's effect will again have a lower timescale than the timescale associated with radiative heating.

4.3 μ CTD Profiles

The 18th of January shows good profiles where surface cooling and solar heating influences are observed at the same time in a competitive way.

A value of $\lambda = 5 \text{ m}$ is chosen based on the monthly average Thetis measurement made for the month of February 2020. μ CTD and meteorological data were merged to create the profiles shown in figure 4.4. Low wind conditions ($< 2 \text{ m s}^{-1}$) have been recorded by the meteorological station for most profiles.

The profiles were taken starting at 9:35 UTC time (11:35 local time: UTC+2). The water column

Figure 4.4 – Click on the figure to animate it, hold to pause. μ CTD structure of temperature on the 18th of January 2021. The orange line is the raw data of temperature from the high resolution measurement. Grey line is the smoothed temperature using the Savitzky-Golay filter (Savitzky, 1964). Meteorological station and Heat fluxes are provided at each timestep. Wind is in ms^{-1} , H_0 and H_{SW} are in Wm^{-2}

already received some shortwave radiation during a certain period of time before, but not sufficient enough to stratify the system; the water column is still fully mixed. The column state at 9:35 has yet some balance between shortwave radiation and surface cooling ($R = 1.69$). Between 9:35 and 11:50, profiles show something that can be interpreted as the signature of shortwave radiation with a rising temperature between 1 m and 8 m depth. In particular, small increase of temperature can be visible at approximately 6 m depth at 10:31. This heated parcel will eventually form a rising parcel of water and additionally suggesting that the light extinction depth approximated in section 2.4 is probably well estimated. Convection can be considered as a slow process, rising/sinking plumes have an order of magnitude of $\mathcal{O}(1) \text{ mm s}^{-1}$ (Bouffard and Wüest, 2019), but can be responsible for moving large parcels of water. If we imagine that this hot parcel of water was formed around 6m, and considering a plume's velocity between 1 and 5 mm s^{-1} , we can expect that moving parcels will travel during more or less 1 h. The signature of the same convective plume is therefore possible to observe between two temperature field measurements and confirm the fact that what we observe between 10:51 and 10:01 can be the consequence of a rising plume.

In the morning, surface cooling is still a leading forcing affecting the very surface layer, forming cold water parcels at the surface. The R ratio fluctuates between 1 and 2 during this period of time. From 11:50 to approximately 15:23, radiative heating dominates the surface layer, leading to a stratified water column.

The profile at 14:22 shows a localized change of H_{SW} . This variation of nearly 100 W m^{-2} is probably an anomaly that can be explained by multiple factors, like a bird making shadow on the sensor or a cloud. During this period of time, R is between 0.36 and 0.87 if the meteorological station measurement at 14:22 is not taken into account.

From 15:44 to 16:31, radiative heating decreases drastically, the R ratio is increased, surface cooling gaining importance on the system and forming cold water parcel at the boundary with the atmosphere.

At the end of the day, similar profiles than the one seen in the morning are recorded. The R ratio is over 2, reaching a value of 27.66 at the end. The thermal stratification around 2 m depth is not due to actual shortwave radiation, but because of the previously stratified system.

In the frame of this work, more profiles were analyzed, showing also similar temperature profiles:

- 8th of January 2021 was a clear but windy day ($\approx 5 \text{ m s}^{-1}$) where 20 temperature profiles were observed. From 10:58 to 14:21, the system stayed fully mixed during the observation time, with an R value varying between 0.8 and 1.5.
- 5th of February 2021 was not windy ($< 1 \text{ m s}^{-1}$) and 44 temperature profiles were taken starting at 7:24 and finishing at 14:22. Surface cooling was quite low ($\approx 60 \text{ W m}^{-2}$) and R was between 0.5 and 8.

- 17th of March 2021 was not windy ($< 2.5 \text{ ms}^{-1}$) but had low temporal coverage, starting at 9:58 and finishing at 12:28. R was between 0.6 and 1.3.

In general, R values lower than 0.8 resulted in stratified profiles and values higher than 2 showed a fully mixed profile without sign of radiative heating.

4.4 Statistical analysis

The steady state model gives a first approach on the relation between those forcing parameters influencing the convective regimes. Given the long-term data available, it is possible to identify when and how persistent are those conditions present along the year. First, we are going to analyze those conditions assuming a range of $R \in [0, 1]$. Consequently, given the result of the μ CTD measurement, another analysis following the same methodology will be carried out based on a different R range.

4.4.1 Annual statistics

The balanced conditions explained in table 3.1 are tested for each long-term measurements and are displayed in figure 4.5.

The radial distance corresponds to the magnitude of surface cooling (H_0). The more a point is situated away from the center, the more surface cooling happens. Low amount of measurement showed low surface cooling heat flux (low amount of points in the inner circle). In fact, heat fluxes computations show only 4 different days in the year (2020-2021) where H_0 is negative in winter (surface heated by the air). Surprisingly, the end of summer is showing a numerous amount of events where surface cooling could be greater than 150 W m^2 .

Color of points determine the amount of shortwave radiation measured. For any season, it appears that surface cooling and shortwave radiation seem to have a positive correlation; when surface cooling decreases, shortwave radiation also decreases. This is due to the fact that, if a point is displayed, it means that it has to satisfy $R \in [0, 1]$. Naturally, we are forcing a positive correlation by defining a ratio between the two heat fluxes. Points seems to be more red and orange during summer and spring. In fall and winter, points tends to be more red, dark red, or black. It looks like the conditions on R , wind and mixing layer seems to be satisfied under lower solar injection in winter/fall than spring/summer,

A point has a bigger size if several measurement satisfying the conditions are detected on the same day. In other words, if conditions are fulfilled persistently in a day, the point will be bigger. Small points are detected for each seasons. Bigger points are visible in summer, fall and winter, spring is showing only few small points. Lines of big points suggests that multiple 10 minutes are persistent within one day.

Occurrences satisfying the balanced condition increases its frequency in fall (OND) with 519

H_0 (W m^2) for days satisfying the conditions in 2020-2021 :
 Wind < 2 (m s^{-1}), $h_{mix} \in [5, \text{inf}]$ (m), $R \in [0,1]$

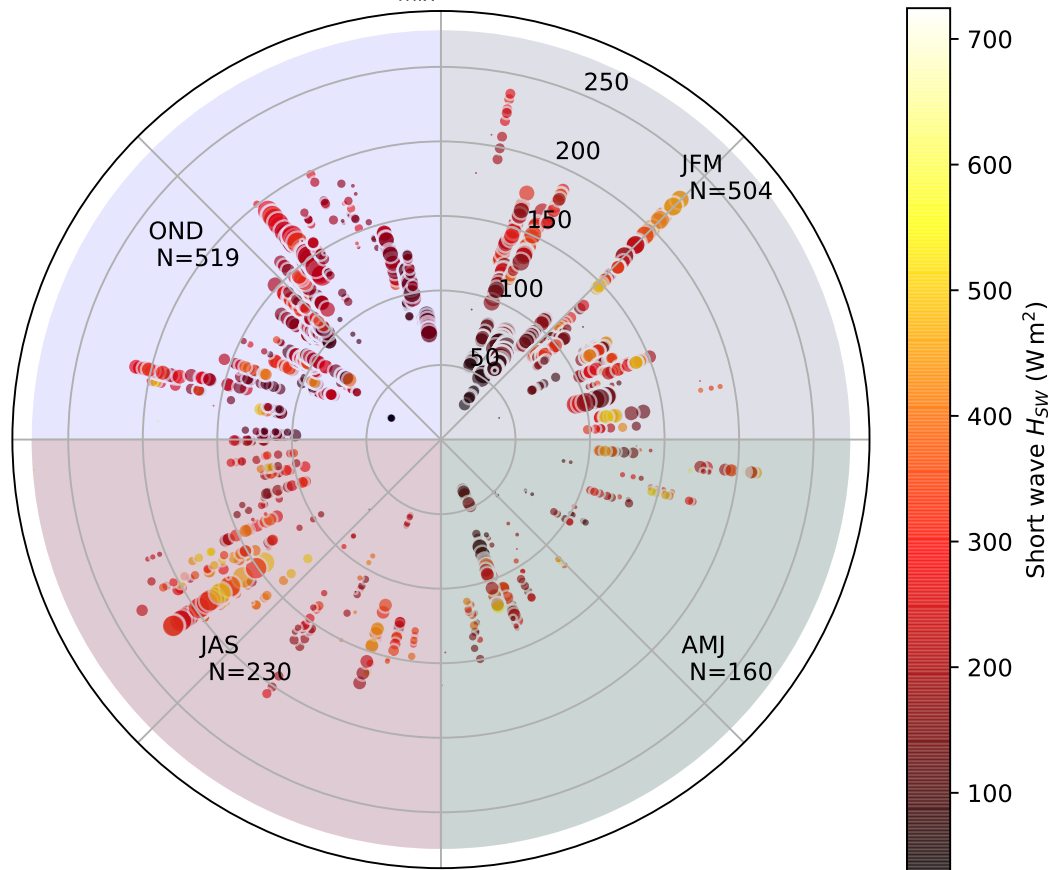


Figure 4.5 – The Polar Chart is separated into four distinct timelines. Each dots represents an event of 10 minutes where specific conditions are satisfied. An event is represented when there is: no wind (less than 2 m/s), the lake is not stratified (the depth of the mixing layer is more than 5 m), N is the number of occurrences in each seasons: winter (JFM), spring (AMJ), summer (JAS) and autumn (OND).

occurrences (86.5 h) and in winter with 504 occurrences (83.8 h). Note that it is the second half of summer that shows the bigger amount of event, making the month of September interesting by fulfilling these conditions.

The repartition of events during the month of winter is different from fall. These two seasons have nearly the same amount of occurrences, but events in winter are often following a straight line and are more grouped than in fall. A possible interpretation would be that conditions are fulfilled more punctually but in a persistent way. Catching this transition regime in winter probably means that this regime will stay for a relatively long period. It is also possible that windy days may affect differently each seasons, making the interpretation of the number of occurrences more difficult.

4.4.2 Consecutive events within a day

With an R ratio between 0 and 1, we want to localize in time where this transition regime happens in the year and during the day. With figure 4.6, we are trying to answer the question of how persistent this transition regime is within a day by highlighting the size of the points of figure 4.5. Additionally, the continuous behavior of the events is investigated. From the analysis we made before on steady state condition, it is possible that the transition regime may happen continuously twice a day: during the morning and during the evening.

From figure 4.6, it seems that the cumulative time (blue bar) within a day does not reach more than 4:30. Most of the other days, conditions are satisfied during less than 3 h in a day. As suggested by the size of the points in Figure 4.5, we have many events occurring in a single day during summer. This day is represented by the long bar on the bottom left of the figure.

In general, long bars are for the majority not entirely filled with red. As suggested by figure 4.5, winter seems to have the longest continuous events (longer red bar).

The day 18th of January 2021, events fulfilling the conditions lasted for approximately 2:40 (2:20 continuously).

Hours of events by day satisfying the conditions in 2020-2021 :
 $\text{Wind} < 2 \text{ (m s}^{-1}\text{)}, \quad h_{\text{mix}} \in [5, \text{inf}] \text{ (m)}, \quad R \in [0,1]$

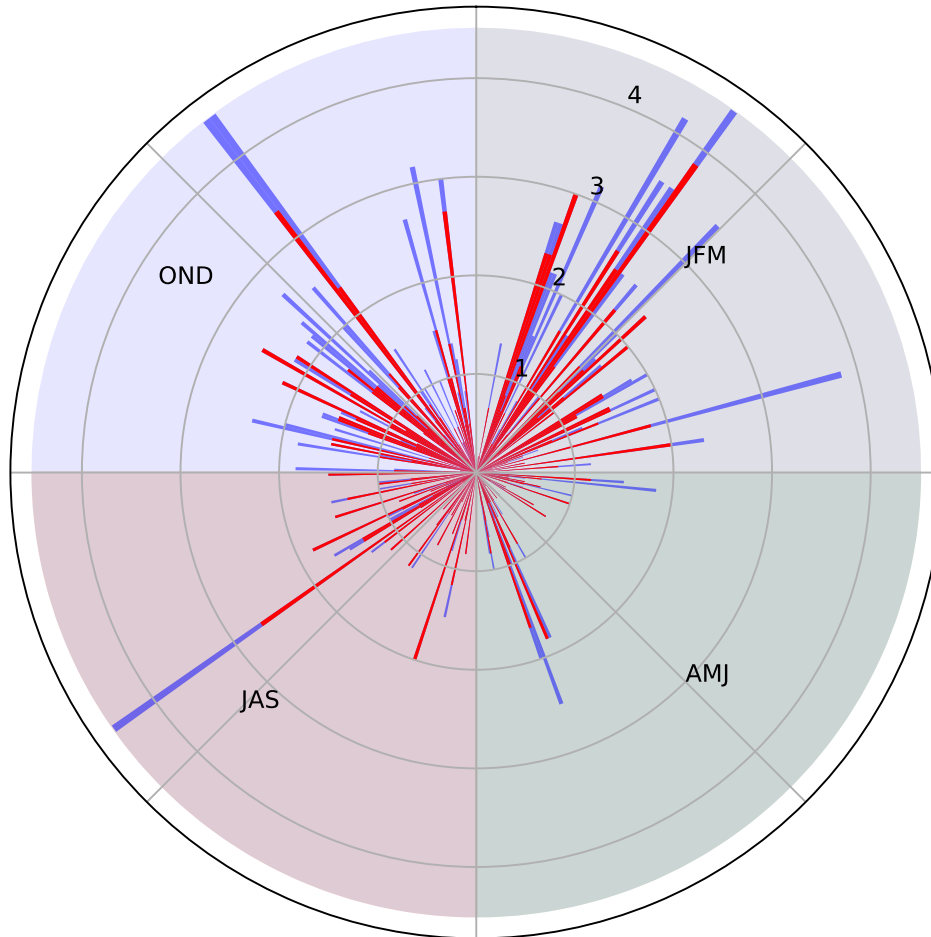


Figure 4.6 – Each bar is a day in which at one or multiple events took place. The radial axis is the time in hours of the events in a day. The more events there is within a day, the longer will be the bar. if conditions are fulfilled continuously in a day, the bar is filled in red.

4.4.3 Daily statistics

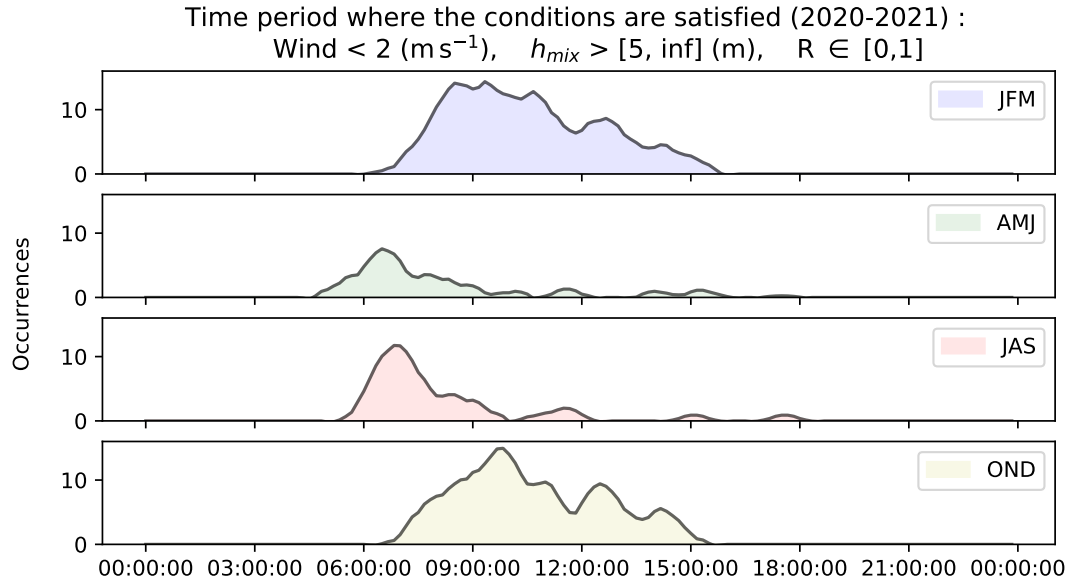


Figure 4.7 – Daily Statistics for each seasons. Occurrences refer to the number of 10 min events where the transition regime conditions are fulfilled. These plots are smoothed using a Savitzky–Golay filter with a window size of 9 and a polynomial order 3.

The transition conditions are fulfilled at different time of the day depending on the season as shown in figure 4.7.

In winter and fall, events are distributed in the whole day, with a drop at midday because the water column is stratified. For the period in spring and summer, events still happen but only early in the morning, mostly because of the fact that the water column quickly get stratified and stay as it is for the rest of the day.

4.4.4 Empirical based transition regime

The μ CTD measurements is showing what we defined as transition regimes profiles but with a different R range than the one deduced from the steady state analysis. From an empirical point of view, It looks like the transition R range should satisfy $R \in [0.8; 2]$. By updating the R range following that statement, it is possible to do a similar statistical analysis.

Results from the polar graph shown in 4.8 show the same behavior than the previous analysis: There is a higher number of events in fall ($N = 561$), a numerous amount in winter ($N=391$), and a low amount in summer ($N = 133$) and spring ($N = 127$). There is one day in summer and one day in spring where the conditions are fulfilled more than usual (bigger points), but are still very punctual.

H_0 (W m^2) for days satisfying the conditions in 2020-2021 :
 Wind < 2 (ms^{-1}), $h_{mix} \in [5, \text{inf}]$ (m), $R \in [0.8, 2]$

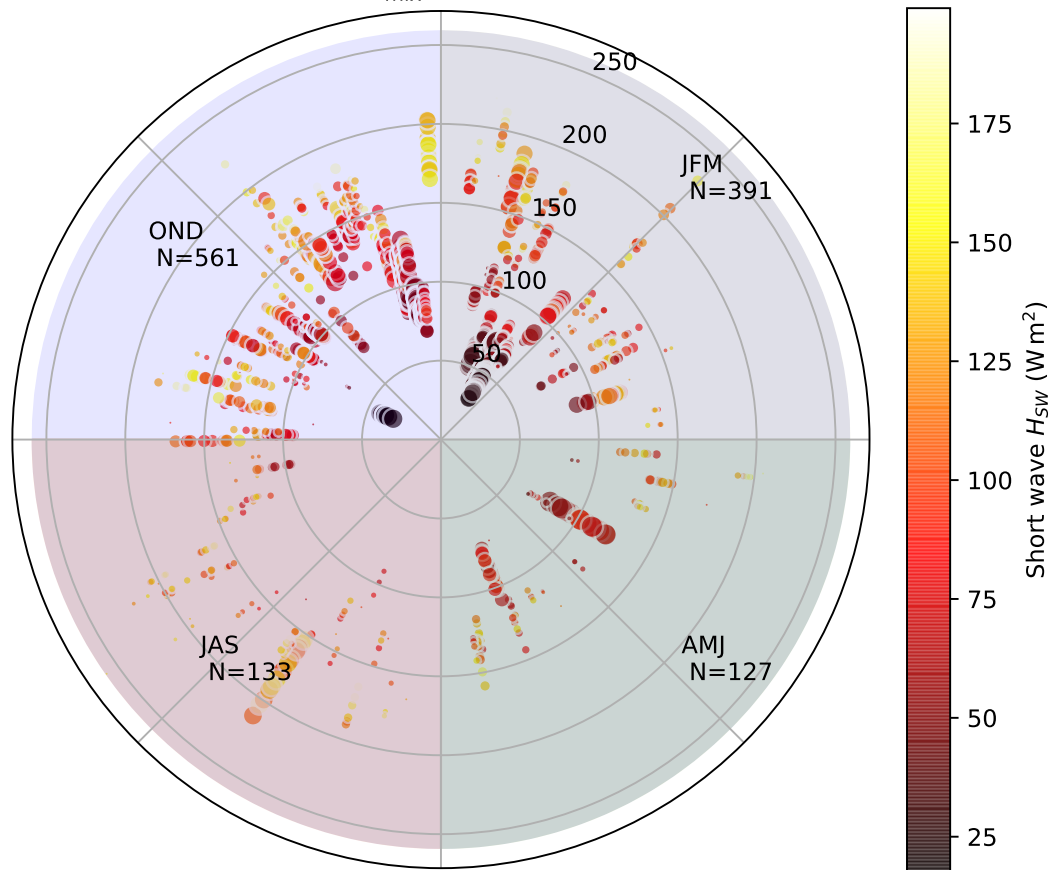


Figure 4.8 – Updated polar chart (figure 4.5) considering $R \in [0.8; 2]$

Hours of events by day satisfying the conditions in 2020-2021 :
 $\text{Wind} < 2 \text{ (m s}^{-1}\text{)}, h_{\text{mix}} \in [5, \text{inf}] \text{ (m)}, R \in [0.8, 2]$

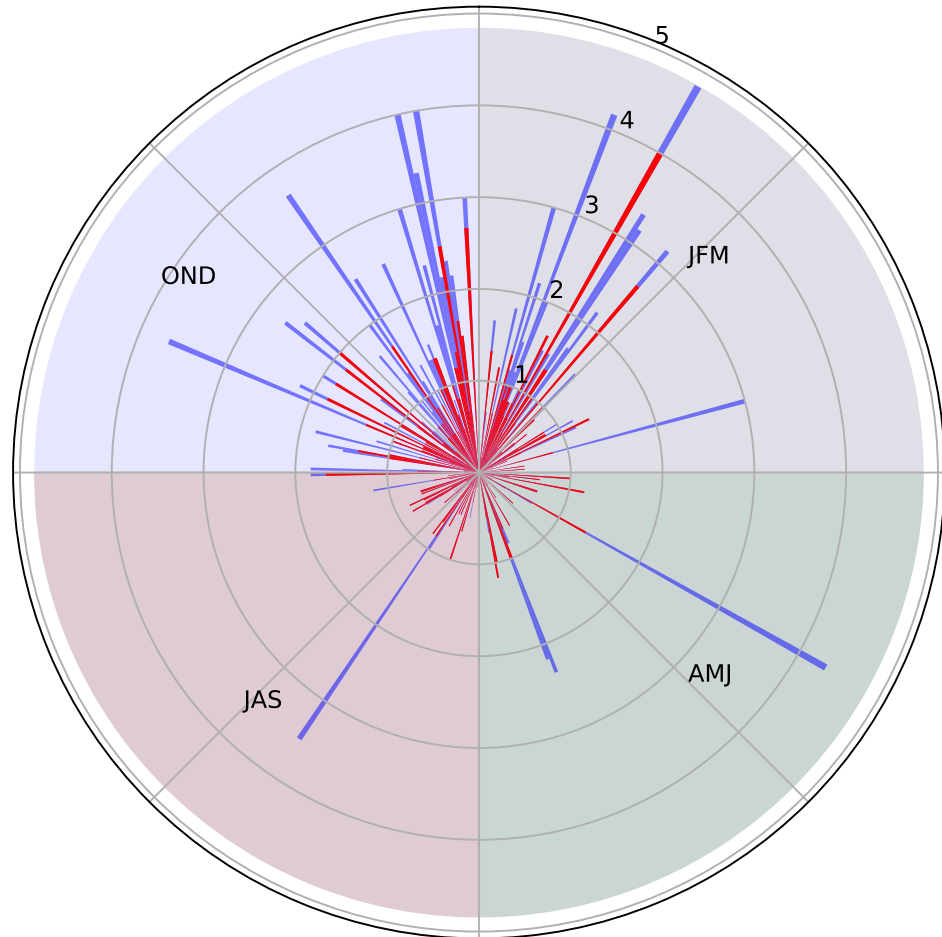


Figure 4.9 – Updated polar bar (figure 4.6) considering $R \in [0.8; 2]$

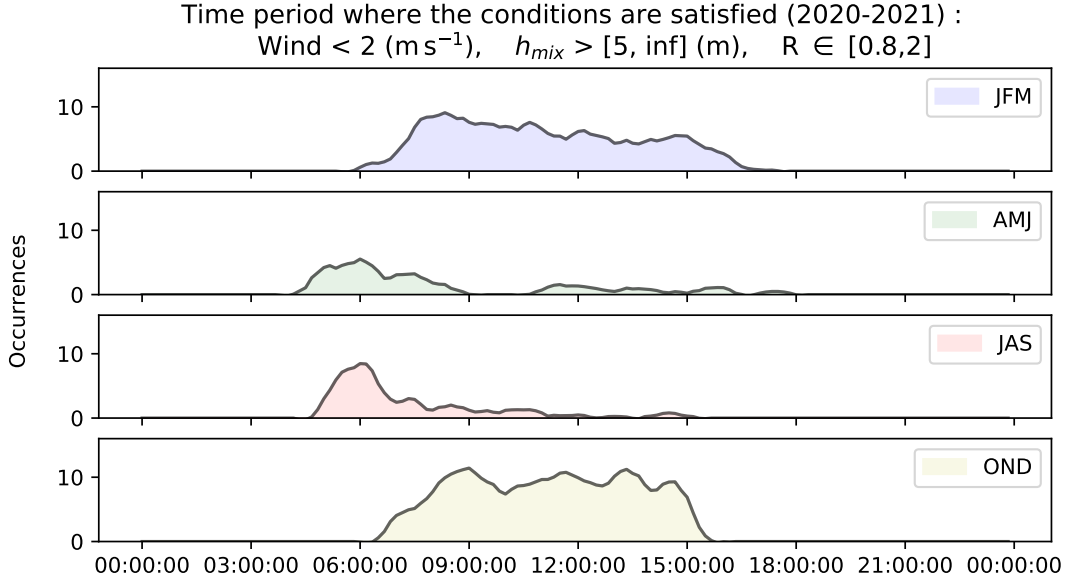


Figure 4.10 – Daily statistics for the empirical R range ($R \in [0.8; 2]$)

The polar bar plot in 4.9 does not show numerous consecutive events (red bar) for any particular season. The day where the consecutive events is maximum (during 4 h) happened on the 30th of January. On the 18th of January 2021, events fulfilling the conditions lasted 2:10 (1 h continuously).

As we can see in the daily statistics in figure 4.10, we may record this event more concentrated in time during September, whereas it is much more sparsed during winter and fall. By doing this statistical analysis, we are not only trying to determine the recurrence of an event satisfying those conditions, but also making an assumption on when to perform a microstructure measurement to catch a convection regime. For example, It may happen that there are less events during summer than fall. However, if the goal is to measure a temperature profile showing a potential interesting convective regimes, one can have the same chances to see it at 6 in the morning in summer than during the entire day in fall.

Under the assumption that the corresponding transition temperature profile happens with an $R \in [0.8; 2]$, the statistical analysis demonstrates that this phenomena is quite persistent in the year.

4.5 Numerical model

Figure 4.11 shows the output of the numerical model, considering day 18th of January 2021. The numerical model is built considering:

- Dimensional heat equation presented in equation 3.4 with Dirichlet boundary condition

at the bottom and Neumann boundary condition at the top of the water column. Bottom boundary condition is updated each 10 min to match the observed bottom temperature.

- Varying κ_T with depth and time measured with the μ CTD profile every 10 min.
- Varying surface cooling (Q_0) and solar injection (H_{SW}) based on computed heat fluxes every 10 min.
- Three different simulations were performed, considering different mixing regimes: 1) without mixing, with mixing (based on 3.46) every 2) $\Delta t = 1$ min and 3) timestep proportional to $\tau_{conv} \approx 30$ min.
- A light extinction length scale of $\lambda = 5$ m.

The timestep of the model is set as $\Delta t = 60$ s. Difference between the displayed modelled and measured profiles will have a maximum time difference of one minute. The vertical resolution is set as $\Delta z = 0.01$ m. The model will start with the constant temperature profile at $t=9:35$. Each profile are displayed every ≈ 10 min, when forcing conditions and diffusivity are updated.

The black curve is the temperature profile corresponding to the high resolution smoothed μ CTD measurements. The dashdotted black curve is the mixed temperature profile assuming that the profile will mix within the mixing layer every 30 min ($\tau_{conv} \approx 30$ min). The dashed black curve corresponds to the modelled temperature profile without any mixing. The dotted black curve is the mixed temperature profile assuming a mixing at every timestep $\Delta t = 1$ min.

Between 9:35 and 10:31, all three modelled temperature profiles give reasonable results comparable to the measured one. In the morning, R is higher than 1, surface cooling being the dominant heat flux. From 10:43 to the end, the three modelled and the observed temperature profiles have a stronger difference. It seems that the model struggles to reproduce effect of stratification occurring due to the increase of shortwave radiation. It is interesting to notice that the mixing depth seems to not be correctly reproduced or calculated: from 13:12 to 15:23, the calculated mixing depth seems to be situated around 5 m, whereas the observed temperature profile seems to show a mixing depth around 3 m. This overestimation seems to affect in particular the two mixed profiles.

The turbulent diffusivity (κ_T) is highly variable and is situated within a range going from 10^{-1} to $10^{-5} \text{ m}^2 \text{ s}^{-1}$ depending on time and depth. In general, κ_T decreases with depth. If the system is stratified, κ_T will tend to decrease locally. Minima of κ_T often match roughly the apparent mixing depth of the measured profile. Overall, the mixing depth seems to be well estimated by the model. However, temperature over that mixing depth are cooler in the modelled profiles than the observation. We can ask ourselves if κ_T is responsible for this difference. Increasing κ_T will increase heat fluxes at a specific location. By decreasing κ_T at the mixing depth, we are localizing more the surface cooling happening at the surface. κ_T is governing how heat fluxes are transferred, but here, this difference makes us think that it is a possible error in the values of Q_0 or H_{SW} .

Figure 4.11 – Click to animate, hold to pause. Measured (solid black) temperature profile is shown. In parallel, the dotted and dashdotted black curves corresponds to the the temperature profile where the mixing algorithm is applied at every timestep and τ_{conv} respectively. The dashed black curve corresponds to the temperature profile without any mixing. The red dashed line corresponds to the smoothed turbulent diffusivity from measurements. The R ratio, surface cooling, shortwave radiation and wind are also displayed at the time when the modelled and measured temperature are plotted. Light extinction depth is set as $\lambda = 5m$ As the time resolution is set at one minute, no more than one minute is elapsed between the modelled profiles and the measured one.

The MSM value is calculated for each timestep between the three modelled profiles and the observed temperature profile. The mean MSM value (\overline{MSM}) is also calculated for each model mode. The corresponding \overline{MSM} for each simulation is 0.49 for the model mixed at every Δt , 0.55 for the model mixed every ≈ 30 min and 0.42 for the model without mixing. A net increase in MSM is seen in the mixed model after 12:32, when the water column starts to get stratified. For the two other models, variations of MSM are too high to be either described or interpreted.

Overall, the modelled profiles give good results for every depth if the observed water column is fully mixed (i.e at the beginning of the day). The model without mixing and with a mixing proportional to τ_{conv} tend to produce the shape of the transition regime, in particular when shortwave radiation increases and the system had time to evolve. By mixing at every timestep, the resulting temperature shape is constant over the mixing depth but still gives interesting results. If the observed water column gets stratified, each of the models tends to overestimate temperature at greater depth than 3 m (by approximately 0.02°C), and underestimate it at the surface (by approximately 0.1°C for the model without mixing). In general, an increase of mixing events gives in this case a better approximation of the near-surface temperature by increasing it, but depreciate the shaping due to competition between surface cooling and shortwave radiation.

5 Discussion

From a simple approach, we can understand and characterise the transition regime and deduce a range for R , allowing a better interpretation of this phenomena by neglecting certain aspects. However, it is important to keep in mind the reasons why the steady state analysis is not sufficient to approach the temperature profile seen by the microstructure profiler. High resolution measurements suggests that the R ratio range for this transition regime to happen is different from the one deduced by the steady state analysis: $R_{SS} : [0; 1] \neq R_{\mu\text{CTD}} : [0 + \delta_1; 1 + \delta_2] \approx [0.8; 2]$ with R_{SS} being the R ratio range approaching the transition state based on the steady state analysis, and $R_{\mu\text{CTD}}$ the R range based on the empirical microstructure measurements. δ is the factor responsible for the difference between the two ranges. Several explanations concerning this δ being not null is discussed below.

5.1 Steady State solution interpretation and its limitations

From the steady state analysis, we could derive a simple analytical solution of the temperature profile, assessing the relative importance of surface cooling and the penetrative shortwave radiation based on R and its resulting temperature profile. Based on the dimensionless heat equation and this R ratio, an analytical solution for the thickness of the diurnal mixed layer and the compensation depth is investigated, giving valuable information on heat and mass transfer changing on a daily basis.

By definition, steady state considers that the system is not changing anymore with time. However, physical processes represented in the steady state equation like surface cooling and radiative heating have their own timescales, both having an order of magnitude of $\mathcal{O}(10^1)$ h (equation 3.20 & 3.18). Natural processes are dynamic; by assessing that physical processes investigated here have timescales, we emphasize the fact that time is a major component in defining the state of the system, in particular for such long processes. More than the physical processes timescales, measurements show very dynamic profile with a lot of variation in terms of solar radiation and surface cooling within a day. Considering the emphasis given to the daily timescale, we can assess that the steady state will never be reached during daytime.

5.2 Timescales

In the frame of this work, we are more interested in the daily timescale than the seasonal one. By defining the effect of surface cooling or radiative heating, we are considering the diurnal mixing layer approximately more or less equal to 10 m (deduced broadly by the microstructure measurements on the 18th of January 2021). However, the daily path shown in figure 4.3 would probably be different for another season. For instance, fall being an overturning season for stability, it is possible that surface cooling would penetrate deeper, making the h/λ ratio have a broader range.

In the analysis, we fixed λ to 5 m. Lake Geneva is subjected to high variation in turbidity due to multiple factor like primary production or the intrusion of the Rhone river. Turbidity is therefore dependent on space and time. The ratio h/λ is defined because these two components are closely related: if turbidity increases, the system will more rapidly stratify and the diurnal mixing layer will reach a low value in a short amount of time. In that case, the h/λ ratio would be more sensitive and quickly reach very low values in a short time. It can also happen that R would never be lower than 1, typically in winter conditions. The timescale analysis is therefore more or less accurate for Lake Geneva depending on time and location.

5.3 μ CTD temperature profiles

Observations can hide physical processes, or show that the system studied cannot be defined by a few mathematical equations. By merging microstructure observations and heat fluxes data, we realised that the R range for the transition state to happen is different from the one deduced by the steady state analysis.

It is important to notice that by using direct and high resolution measurements, macroscopic and microscopic phenomena can also be captured. On a microscopic scale, turbulence can be seen but should be responsible for lower temperature variations. On a more macroscopic one, a rise of temperature can be the result of a rising plume. It is important to keep in mind that the instrument is measuring a water column (1D) and taking a snapshot of reality. Convection is a continuous three dimensional phenomena, sometimes unpredictable, observations should therefore be treated accordingly.

The 18th of January 2021 is chosen for its low wind conditions, time coverage and most importantly because interesting shapes (due to competition between heat fluxes) were recorded during a certain period of time. However, clouds were present this day in the atmosphere and could have influenced the R value by making the quantification of heat flux subject to more errors.

We designated a new range for R based on observations. However, only few profiles were analyzed and were specific for a particular season (winter). This empirical R ratio can therefore be subjected to errors due to the possible seasonal bias. The transition regime defined by the

empirical R ($R_{\mu\text{CTD}}$) is highly uncertain. What is more consistent however, is that values of R lower than 0.5 resulted most of the time in the formation of a stratification regime, which is supported by the timescale analysis, saying that the effect of radiative heating will happen faster than the effect of surface cooling with a R under 0.5.

As in many researches exploring the mixed-layer heating and deepening in lakes (Farmer, 1975), lateral advection is also neglected here, but can influence thermal structure and evolution of the mixed layer in a significant way (Bouffard and Wüest, 2019, Doda et al., 2021).

5.4 Numerical model interpretation and limitations

By comparing the modelled and observed microstructure temperature profiles, we are able to explain certain aspects responsible for the difference between the two. The most striking one is the overestimation and underestimation of the water temperature during the stratified period for depths lower than 3 m and higher than 3 m respectively. This deviation may come from an error in the R ratio, i.e in the heat fluxes values. Indeed, modelled profiles (specially the one without mixing) seems to be influenced by surface cooling in an excessive way. The fact that temperature is overestimated at higher depth can arise from an overestimation of the radiative heating component or of the light extinction depth scale. One possible reason for this error is the cloud cover consideration in the heat flux computation, and is investigated more in details below.

Cloud cover

By analyzing more in-depth how solar radiation and surface cooling heat fluxes are generated, we can assess the possible errors present in these components. By computing heat fluxes uses daily scale cloud cover to provide a 10 min resolution as an output, resulting in a possible bias. However, it is complicated to model the impact of cloudiness on shortwave radiation and cooling because of the fact that the G term in equation 3.50 is implicitly taking into account cloudiness.

The numerical model is not taking R as an input, but the shortwave radiation and surface cooling separately, as they are not treated identically in the implicit scheme (equation 3.45). The temperature profiles of the three modelled profiles suggested a possible overestimation of surface cooling and an underestimation of shortwave radiation during the afternoon, when the water column is stratified.

This error may be partly responsible for the δ introduced to define the R range difference between the observations and the steady state solution.

Other aspects

Although the numerical model takes into account the unsteadiness component, it is still a simplified model based on the heat equation with a source term. Natural phenomena are dynamic, rising and sinking plumes are probably generating relatively high variation in the temperature profiles. By taking into account advection in the turbulent diffusion term, the developed numerical model is omitting some aspects of advection like these water parcels displacement. This mixing is reproduced by the mixing algorithm presented. The models are not reproducing these moving parcels, but averaging temperature over the mixing depth, leading to more coherent profiles (higher \overline{MSM}). Based on the estimation of the convective timescale τ_{conv} , we decided to mix in a discrete way every ≈ 30 min. Considering that the system is mixing at each timestep $\Delta t = 1$ min (corresponding to the model time resolution) would be assuming that the convection timescale is equal to time resolution of the model. However, by discretising the mixing phenomena, we are in some way omitting that convection act in a continuous way. In a same way, we are updating forcing parameters Q_0 and I_0 each 10 min due to data time resolution, changes in solar radiation and surface cooling is obviously continuous, and can change drastically within a 10 min range. Finally, results showed a slightly higher \overline{MSM} for the model mixed every ≈ 30 min. This mean is however difficult to interpret due to its high variability between each displayed profiles.

By choosing and implementing a simplified model, generated profiles demonstrated that shapes corresponding to the transition regime were actually reached for a large range of R . It is probably because that the system is mixing vertically and horizontally that those profile are difficult to capture. This statement can make us think that these transition profiles can happen more often than we think, but can not be observed due to other natural aspects like lateral and vertical mixing, wind and others.

5.5 Statistical analysis

The statistical analysis gives informations about the persistency and the temporality of a phenomena satisfying conditions based on wind velocity, the calculated mixing layer and the R ratio. Two sets of conditions were analyzed to identify the transition regime on an annual and daily basis. One of them is based on the steady state analysis, and the other on empirical observations. The fact that this empirical R range is based on a low amount of observations made in winter can result in a bias, especially in the case where this range is extrapolated on an annual basis. It is probable that R is not the only factor responsible for this observed transition temperature shape.

For both threshold conditions on R , more events were recorded during the period of fall and winter. In fall, the air temperature decreases, and the lake is still warm from the past summer. The lake is nearly always cooling and solar radiation is probably not strong enough to make the system stratify on a daily basis. On the contrary, in summer and spring, the lake is probably very quickly stratified due to the high increase of solar radiation. The lake is also probably cold

at high depth, making it very stable.

Whether in winter or in summer, Lake Geneva is very often cooling at the surface. The competition between surface cooling and shortwave radiation may therefore happen in every season, but last shorter in summer than in winter.

By making this analysis, an algorithm in which any threshold on wind, surface cooling, radiative heating or the mixing layer depth can be set as an input. In the frame of this thesis, we were specially focused on the transition regime, but period of stratification or period of high surface cooling could also have been studied.

This statistical analysis assess, for both R (empirical or steady state based), when and how persistent radiative heating and surface cooling act in a competitive way on the water column under low wind conditions. These thresholds may not lead each time to the transition state, but have to be seen as a probability in which this state can be reached.

6 Conclusion

At a daily time scale, a temperature profile can switch from a fully mixed to an entirely stratified state. The state in between these two regimes is defined as a transition regime and is investigated in this study. We defined that the principal causes for this regime to happen is most certainly due to a competition of shortwave radiation and surface cooling, here represented by the R ratio. While surface cooling acts as a boundary flux forming a cold parcel of water at the top and leading to unstability, solar radiation acts as a volumetric heat flux, heating and thus stabilizing the system. These two heat fluxes may therefore influence the water at a comparable scale but at different locations in the water column, modifying the compensation and mixing depth and forming a unique shape in the temperature field. As these physical components are highly variable in time, this transition regime could last for a few minutes or a few hours but seems to be persistent along the year. Following the long-term data analysis, it has been deduced that the occurrence of this transition regime would behave differently depending on the season. With high resolution measurements, this shape can be observed and put in relation with the heat fluxes acting on the system. Two main results were given by these precise measurements: the temperature profile's shape corresponding to the transition regime, and the range of R where this shape is forming. In parallel, a detailed analytical analysis is made considering the heat equation assuming steady state conditions. A dimensionless temperature equation is derived, different temperature profile are produced, R being the governing component determining the state of the temperature profile. The observed transition profile is reproduced for an R ratio going from 0 to 1 under steady state conditions. Moreover, a characterization of this transition regime is made by deriving an analytical expression on the compensation and mixing depth depending on the R ratio. A steady state model is simple, an analytical expression can be derived easily and an interpretation can be made, but can differ from observations depending on the timescale of the processes investigated. The effect of radiative heating or surface cooling on the water column is more or less rapid depending on the R ratio or the ratio of the mixing depth and light penetration length, making time an important parameter when it comes to determine the conditions where the transition is happening or not. By building a simple numerical model based on the heat equation with a source term, the system which undergoes constantly changing forcing

conditions is recreated and compared with the observations of the 18th of January 2021, when several transition regimes were recorded. Despite the fact that surface cooling is probably overestimated by the heat flux computation, the model correctly integrates radiative heating, surface cooling and mixing mechanisms, and reacts in a similar way to the observed profiles. Cloud cover's influence on heat fluxes, wind adding a further degree of complexity, the fact that convection is a complex three-dimensional physical phenomena are several elements considered to explain the errors, simplification and limits of this analysis.

By building an intuition over simple models and analysis, a solid basis on this defined transition regime is set. By exploring the competition between cooling and shortwave radiation, it is possible to open new doors to researches about the role of convective regime in vertical heat and mass transfer, specially in a time where climate change due to anthropogenic emissions seems to have a notable impact on lakes (Råman Vinnå et al., 2021, Schwefel et al., 2016).

7 Acknowledgements

Hugo Ulloa and Sebastiano Piccolroaz were not only my supervisors who helped me to find direction or to discuss about the fascinating subjects that came out from this master thesis, they were also inspirational persons whose contagious curiosity about limnology and physics motivated me along the entire semester. I can definitely say that I am seeing lakes with a different eye, and I am very grateful to these two human beings for that.

I would like to further thank Prof. A. Johnny Wüest for his capacity to transmit his passion and ask interesting questions during APHYS meetings, but also for his smile, specially when Switzerland wins a football match. Further thank to Johnny for having built a wonderful team (APHYS), with which I could have the pleasure to have a good times, specially with Guillaume Cunillera, Sebastien Lavanchy, Camille Minaudo, Tomy Doda and Lara Dubois. Finally, I would like to thank my friends here (Alexis, Aurelien, Lorenzo, Alexandre (Michel), Raphael, Nouha, Blanche, Julie, Aurelie) but also those who are far (Joel, Axel, Raphael, Louis & Paulin), my family (Pablo, Claire, Lucas & Gonzalo) and last but not least, Satellite.

Bibliography

- Andersen, M. R., Sand-Jensen, K., Iestyn Woolway, R., & Jones, I. D. (2017). Profound daily vertical stratification and mixing in a small, shallow, wind-exposed lake with submerged macrophytes. *Aquatic Sciences*, 79(2), 395–406. <https://doi.org/10.1007/s00027-016-0505-0>
- Augusto-Silva, P. B., MacIntyre, S., de Moraes Rudorff, C., Cortés, A., & Melack, J. M. (2019). Stratification and mixing in large floodplain lakes along the lower amazon river. *Journal of Great Lakes Research*, 45(1), 61–72. <https://doi.org/https://doi.org/10.1016/j.jglr.2018.11.001>
- Boehrer, B., & Schultze, M. (2008). Stratification of lakes. *Reviews of Geophysics*, 46(2). <https://doi.org/https://doi.org/10.1029/2006RG000210>
- Bouffard, D., & Wüest, A. (2019). Convection in lakes. *Annual Review of Fluid Mechanics*, 51(1), 189–215. <https://doi.org/10.1146/annurev-fluid-010518-040506>
- Doda, T., Ramón, C., Ulloa, H., Wüest, A., & Bouffard, D. (2021). Seasonality of density currents induced by differential cooling. <https://doi.org/10.5194/hess-2021-195>
- Farmer, D. M. (1975). Penetrative convection in the absence of mean shear. *Quarterly Journal of the Royal Meteorological Society*, 101(430), 869–891. <https://doi.org/https://doi.org/10.1002/qj.49710143011>
- Fink, G., Schmid, M., Wahl, B., Wolf, T., & Wüest, A. (2014). Heat flux modifications related to climate-induced warming of large european lakes. *Water Resources Research*, 50(3), 2072–2085. <https://doi.org/https://doi.org/10.1002/2013WR014448>
- Gray, E., Mackay, E. B., Elliott, J. A., Folkard, A. M., & Jones, I. D. (2020). Wide-spread inconsistency in estimation of lake mixed depth impacts interpretation of limnological processes. *Water Research*, 168, 115136. <https://doi.org/https://doi.org/10.1016/j.watres.2019.115136>
- Grishchenko, D. L. (1959). *The dependence of albedo of the sea on the altitude of the sun and disturbance of the sea surface*. (Vol. 80).
- Imberger, J. (1985). The diurnal mixed layer. *Limnology and Oceanography*, 30(4), 737–770. <https://doi.org/https://doi.org/10.4319/lo.1985.30.4.0737>
- Imberger, J., & Hamblin, P. F. (1982). Dynamics of lakes, reservoirs, and cooling ponds. *Annual Review of Fluid Mechanics*, 14(1), 153–187. <https://doi.org/10.1146/annurev.fl.14.010182.001101>

- Imboden, D., & Wüest, A. (1995). Mixing mechanisms in lakes. https://doi.org/10.1007/978-3-642-85132-2_4
- Kirillin, G., & Shatwell, T. (2016). Generalized scaling of seasonal thermal stratification in lakes. *Earth-Science Reviews*, 161, 179–190. <https://doi.org/10.1016/j.earscirev.2016.08.008>
- Laird, N. F., & Kristovich, D. A. R. (2002). Variations of sensible and latent heat fluxes from a great lakes buoy and associated synoptic weather patterns. *Journal of Hydrometeorology*, 3(1), 3–12. [https://doi.org/10.1175/1525-7541\(2002\)003<0003:vosalh>2.0.co;2](https://doi.org/10.1175/1525-7541(2002)003<0003:vosalh>2.0.co;2)
- Minaudo, C., Odermatt, D., Bouffard, D., Rahaghi, D. I., Lavanchy, S., & Wüest, A. (2021). High-frequency lake optical properties response to primary production. *Environmental Science and Technology*.
- Mobley, C. (1994). *Light and water: radiative transfer in natural waters*.
- Moum, J. N. (1996). Efficiency of mixing in the main thermocline. *Journal of Geophysical Research: Oceans*, 101(C5), 12057–12069. <https://doi.org/10.1029/96JC00508>
- Niiler, P. P. (1977). One-dimensional models of the upper ocean. *Modelling and Prediction of the Upper Layers of the Ocean*, 143–172. <https://ci.nii.ac.jp/naid/10025553601/en/>
- Olsen-Kettle, L. (2011). Numerical solution of partial differential equations. *Lecture notes at University of Queensland, Australia*.
- Osborn, T. R. (1980). Estimates of the local rate of vertical diffusion from dissipation measurements. *Journal of Physical Oceanography*, 10(1), 83–89.
- Piccolroaz, S., Toffolon, M., & Majone, B. (2013). A simple lumped model to convert air temperature into surface water temperature in lakes. *Hydrology and Earth System Sciences*, 17(8), 3323–3338. <https://doi.org/10.5194/hess-17-3323-2013>
- Piccolroaz, S., Fernández-Castro, B., Toffolon, M., & Dijkstra, H. A. (2021). <https://doi.org/10.1038/s41597-021-00965-0>
- Råman Vinnå, L., Medhaug, I., Schmid, M., & Bouffard, D. (2021). The vulnerability of lakes to climate change along an altitudinal gradient. *Communications Earth & Environment*, 2(1), 35. <https://doi.org/10.1038/s43247-021-00106-w>
- Reda, I., & Andreas, A. (2008). Solar position algorithm for solar radiation applications (revised). <https://doi.org/10.2172/15003974>
- Savitzky, M., A.; Golay. (1964). Smoothing and differentiation of data by simplified least squares procedures. *Analytical Chemistry*, 36(8), 1627–39.
- Schwefel, R., Gaudard, A., Wüest, A., & Bouffard, D. (2016). Effects of climate change on deepwater oxygen and winter mixing in a deep lake (lake geneva): comparing observational findings and modeling. *Water Resources Research*, 52(11), 8811–8826. <https://doi.org/10.1002/2016WR019194>
- Soloviev, A., & Lukas, R. (2014). *The near-surface layer of the ocean* (Vol. 48). <https://doi.org/10.1007/978-94-007-7621-0>
- Soloviev, A., & Schlüssel, P. (1996). Evolution of cool skin and direct air-sea gas transfer coefficient during daytime. *Boundary-Layer Meteorology*, 77(1), 45–68. <https://doi.org/10.1007/BF00121858>

- Sutherland, G., Reverdin, G., Marié, L., & Ward, B. (2014). Mixed and mixing layer depths in the ocean surface boundary layer under conditions of diurnal stratification. *Geophysical Research Letters*, 41(23), 8469–8476. <https://doi.org/10.1002/2014GL061939>
- Thomas, L. H. (1949). *Elliptic problems in linear difference equations over a network*.
- Thomson, R., & Fine, I. (2003). Estimating mixed layer depth from oceanic profile data. *Journal of Atmospheric and Oceanic Technology*, 20, 319–329.
- Verburg, P., Hecky, R., & Kling, H. (2003). Ecological consequences of warming in lake tanganyika. *Science (New York, N.Y.)*, 301, 505–7. <https://doi.org/10.1126/science.1084846>
- Woolway, R., Jones, I., Hamilton, D., Maberly, S., Muraoka, K., Read, J., Smyth, R., & Winslow, L. (2015). Automated calculation of surface energy fluxes with high-frequency lake buoy data. *Environmental Modelling & Software*, 70. <https://doi.org/10.1016/j.envsoft.2015.04.013>
- Wüest, A., Bouffard, D., Guillard, J., Ibelings, B., Lavanchy, S., Perga, M.-E., & Pasche, N. (2021). Léxplora – a floating laboratory on lake geneva offering unique lake research opportunities. *WIREs water*. <https://doi.org/10.1002/wat2.1544>
- Wüest, A., & Lorke, A. (2003). Small-scale hydrodynamics in lakes. *Annual Review of Fluid Mechanics*, 35(1), 373–412. <https://doi.org/10.1146/annurev.fluid.35.101101.161220>

